A&A 585, A44 (2016)
DOI: 10.1051/0004-6361/201526257

Astronomy & Astrophysics

Dense gas tracing the collisional past of Andromeda⋆

An atypical inner region?

Anne-Laure Melchior[1] and Françoise Combes[2]

[1] LERMA, Sorbonne Universités, UPMC Univ. Paris 6, Observatoire de Paris, PSL Research University, CNRS, 75000 Paris, France
e-mail: A.L.Melchior@obspm.fr
[2] Observatoire de Paris, LERMA, Collège de France, PSL, CNRS, Sorbonne Univ., UPMC, 75000 Paris, France
e-mail: Francoise.Combes@obspm.fr

Received 3 April 2015 / Accepted 12 October 2015

ABSTRACT

The central kiloparsec region of the Andromeda galaxy is relatively gas poor, while the interstellar medium appears to be concentrated in a ring-like structure at about 10 kpc radius. The central gas depletion has been attributed to a possible head-on collision 200 Myr ago, supported by the existence of an offset inner ring of warm dust. We present new IRAM 30 m radio telescope observations of the molecular gas in the central region, and the detection of CO and its isotopes ^{13}CO(2−1) and C^{18}O(2−1), together with the dense gas tracers, HCN(1−0) and HCO+(1−0). A systematic study of the observed peak temperatures with non-local thermal equilibrium simulations shows that the detected lines trace dense regions with n_{H_2} in the range 2.5×10^4−5.6×10^5 cm^{-3}, while the gas is very clumpy with a beam filling factor of 0.5−2×10^{-2}. This is compatible with the dust mass derived from the far-infrared emission, assuming a dust-to-gas mass ratio of 0.01 with a typical clump size of 2 pc. We also show that the gas is optically thin in all lines except for ^{12}CO(1–0) and ^{12}CO(2–1), CO lines are close to their thermal equilibrium condition at 17–20 K, the molecular hydrogen density is larger than critical, and HCN and HCO+ lines have a subthermal excitation temperature of 9 K with a density smaller than critical. The average ^{12}CO/^{13}CO line ratio is high (∼21), and close to the ^{12}CO/C^{18}O ratio (∼30) that was measured in the north-western region and estimated in the south-east stacking. The fact that the optically thin ^{13}CO and C^{18}O lines have comparable intensities means that the secondary element ^{13}C is depleted with respect to the primary ^{12}C, as is expected just after a recent star formation. This suggests that there has been a recent starburst in the central region, supporting the head-on collision scenario.

Key words. galaxies: abundances – galaxies: individual: M31 – galaxies: kinematics and dynamics – submillimeter: ISM – molecular data

1. Introduction

While the outer parts of the Andromeda galaxy exhibit numerous relics of past interactions (McConnachie et al. 2009), the main disc exhibits an enhanced star formation activity in a ring at 10 kpc (Ford et al. 2013) and the central part is atypical. The M31 galaxy hosts a very massive black hole with a mass of 0.7−1.4×10^8 $M_\odot$ (Bacon et al. 2001; Bender et al. 2005) that is one of the most under-luminous supermassive black holes (Garcia et al. 2010), which is surrounded by very little gas (Melchior & Combes 2013). Infrared data and optical ionised gas display a 0.7 kpc off-centred inner ring, and Block et al. (2006) have proposed a frontal collision with M32 to explain this double ring structure. This collision would have occurred 200 Myr ago. In this paper, we present observations of millimetre molecular lines probing dense gas regions along the minor axis in the inner ring. In Sect. 2, we present the data used in this paper. In Sect. 3, we describe the data reduction. In Sect. 4, we describe our results and which physical information we can extract. In Sect. 5, we argue that our results support a 200 Myr old starburst triggered by the frontal collision with M32. For consistency with our previous analysis, we consider a distance of M31 of 780 kpc and a pixel size 1 arcsec = 3.8 pc.

Table 1. M31 observed positions.

Pos	RA (J2000)	Dec (J2000)	$\Delta\alpha$ ($''$)	$\Delta\delta$ ($''$)	T_{int} (min)
I	00 42 29.1	+41 18 03.6	–172.1	115.3	284
I-B	00 42 26.4	+41 17 58.0	–202.5	109.7	173
2d-a	00 42 56.2	+41 14 38.0	133.4	–90.3	262
2d-b	00 42 57.3	+41 14 38.0	145.8	–90.3	204
2c-a	00 42 54.9	+41 14 14.0	118.8	–114.3	79

Notes. We provide the J2000 coordinates, offsets and integration times of the five positions observed.

2. The data

2.1. Millimetre observations

We observed five positions listed in Table 1, which also gives the offsets and integration time. We computed the offsets with respect to the position of the optical centre ((J2000) $00^h42^m44.371^s$ $+41°16'08.34''$) provided by Crane et al. (1992) and used in previous papers (Melchior et al. 2000; Melchior & Combes 2011, 2013). The observed positions lie in the

⋆ Based on observations carried out with the IRAM 30 m radio telescope. IRAM is supported by INSU/CNRS (France), MPG (Germany) and IGN (Spain).

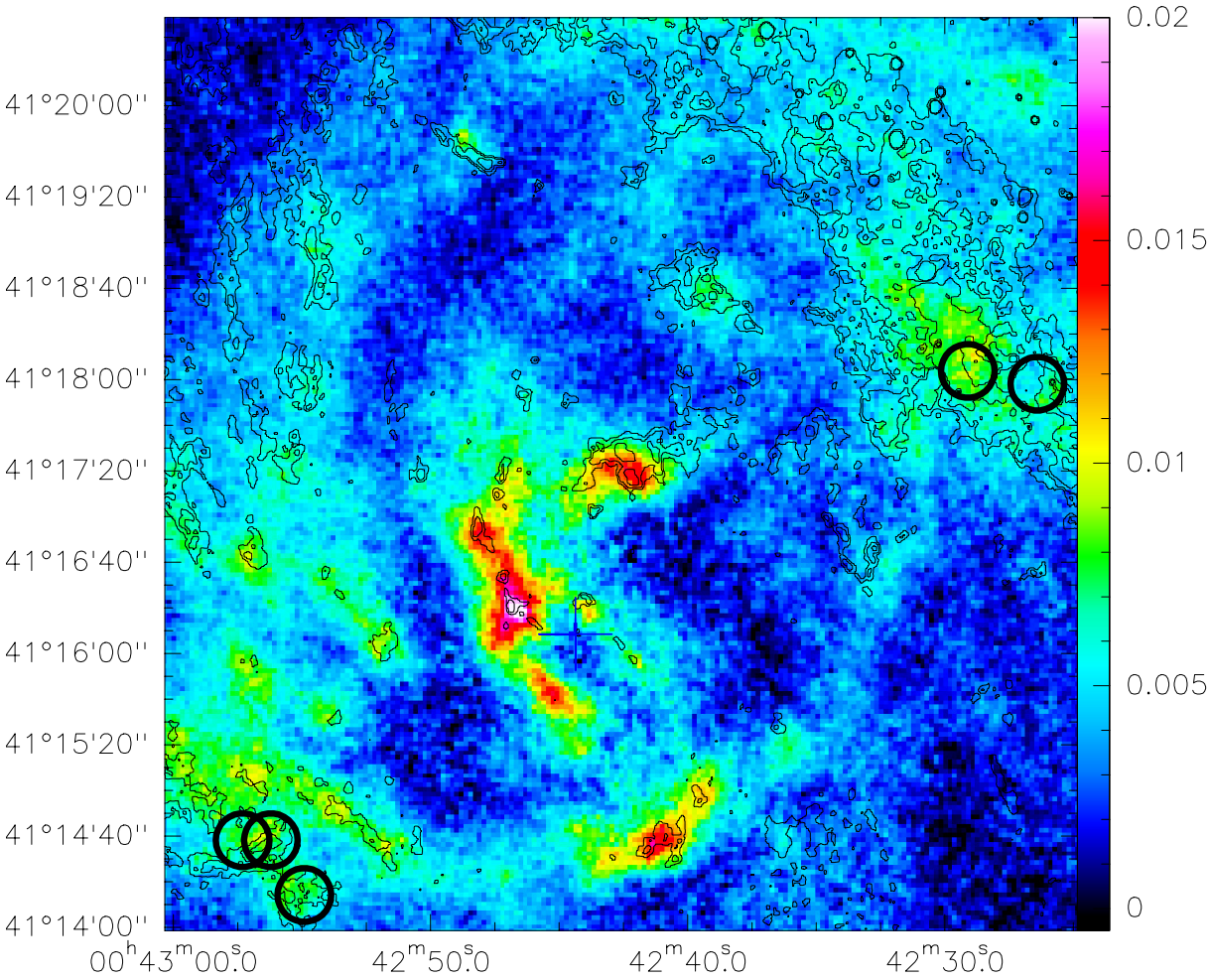

Fig. 1. Positions observed in HCO+(1–0), HCN(1–0) and ^{13}CO(2–1) (and C^{18}O) are indicated with circles superimposed on the *Herschel*/PACS 100 μm map (Viaene et al. 2014). Contour levels (0.05, 0.1, 0.2) correspond to A_B extinction computed assuming all the dust is in front of the bulge as discussed in Melchior et al. (2000). Extinction is underestimated by an unknown factor due to the uncertainties in the geometrical configuration of the gas in this area.

inner 1 kpc ring along the minor axis (of the main disc inclined at 77 deg). The total integration time for each position is provided in the last column. In Fig. 1, these positions are superimposed on the *Herschel* 100 μm map provided by Viaene et al. (2014) and A_B extinction contours computed in Melchior et al. (2000). In the 100 μm and A_B maps, we can see the 0.7 kpc off-centred inner ring.

The observations have been performed with the IRAM 30 m radio telescope equipped with the EMIR receiver in the period 20th–23rd December 2011. They were performed in dual polarisation and the E0/E2 band combination were tuned in order to cover the following frequency bandwidths:

1. 87.4–91.4 GHz and 83.8–87.8 GHz (optimised for HCO+(1–0) and HCN(1–0))
2. 218.65–222.65 GHz and 214.95–218.95 GHz (optimised for ^{13}CO(2–1) and C^{18}O(2–1)).

Two backends were connected to two main receivers: FTS with a spectral resolution of 0.19MHz and WILMA autocorrelator with a spectral resolution of 2MHz. WILMA was non-operational in some observations, and have mainly been used to check the quality of the observations. We smoothed the FTS data to the optimised resolution of 2.1 km s^{-1} up to 34 km s^{-1}. Observations were performed in non-symmetric wobbler mode to avoid sky subtraction from Andromeda's main disc. The azimuthal radius of the wobbler was set to 240 arcsec or set manually, relying on the extinction map of the area (Melchior et al. 2000). As discussed by Greve et al. (1996), large wobbler throws reduce the sensitivity to point sources. However, this is restored to a large extent with an active near-focus correction. It is also possible that some emission is subtracted by the OFF signal. In principle, this would occur at a velocity different from the signal velocity, even though this cannot be excluded given the complex velocity pattern. One can also argue, on the basis of the detections discussed in the next section, that the emitted signal is weak, so the probability of chopping a strong source is small. As shown in the figures discussed below, there is no obvious sign of emission in the OFF measurements, so this is in the worst case a second order effect. In addition, these effects are expected to affect ^{13}CO(2–1) and C^{18}O(2–1) similarly, as well as HCO+(1–0) and HCN(1–0). They could nevertheless affect the normalisation with respect to ^{12}CO(2–1) and ^{12}CO(1–0) obtained independently.

We retrieved ^{12}CO(2–1) and ^{12}CO(1–0) data from previous IRAM observations described in Melchior & Combes (2011, 2013, and in prep.). ^{12}CO(1–0) detection is only available for M31I.

2.2. Infrared data

The five positions observed at IRAM 30 m were observed by *Herschel*/SPIRE instrument. The 1-kpc ring hosts cold

Table 2. Dust properties derived from the infrared data for the M31 observed positions.

	D14				V14					
Pos	$U_{\rm SPIRE350}$	$U_{\rm M160}$	$T^{\rm cold\,dust}_{\rm SPIRE350}$ (K)	$T^{\rm cold\,dust}_{\rm M160}$ (K)	$T^{C}_{\rm dust}$ (K)	$T^{W}_{\rm dust}$ (K)	$M_{\rm dust}$ ($10^3\ M_\odot$)	M_* ($10^7\ M_\odot$)	SFR ($M_\odot$/Myr)	τ_v
I	1.53 ± 0.21	2.1 ± 0.5	19.3	20.3	20.	42.	2.90	3.2	3.3	0.52
I-B	1.52 ± 0.02	1.3 ± 0.3	19.3	18.7	20.	57.	2.86	2.5	2.8	–
2d-a	2.73 ± 0.37	2.6 ± 0.5	21.3	21.1	23.	34.	0.98	3.2	13.4	–
2d-b	1.78 ± 0.15	2.6 ± 0.5	19.8	21.1	23.	34.	0.98	3.2	13.4	–
2c-a	2.07 ± 0.40	3.1 ± 0.4	20.3	21.8	23.	–	1.49	3.5	16.1	1.89

Notes. In the second and third columns, we provide the mean starlight heating rates provided by Draine et al. (2014, D14) for two different resolutions (24.″9 and 39″) at the pointing positions. In the fourth and fifth columns, we present cold dust temperatures derived from these mean starlight measurements. In the sixth through tenth columns, we provide cold and warm dust temperatures, dust and stellar masses, star formation rates and dust optical depths computed by Viaene et al. (2014, V14) at these positions in 36″ pixels.

Table 3. Properties of the main lines in the two observed bands.

Transition	*HPBW* (arcsec)	$\eta_{\rm mb}$	ν_0 (GHz)	δv (1 MHz) (km s^{-1})	$E_{\rm up}$ (K)	$A_{\rm ul}$ s^{-1}	$C_{\rm ul}$ (cm^3 s^{-1})	$n_{\rm c}$ (20 K) (cm^{-3})
SiO $J = 2 \rightarrow 1$	28.	81	86.847	3.5	6.25	2.93×10^{-5}	1×1^{-10}	2.93×10^{5}
C_2H $N = 1 \rightarrow 0$	28.	81	87.329	3.4	4.19	0.26×10^{-6}	5.19×10^{-12}	5.01×10^{4}
($J = 3/2 \rightarrow 1/2$, $F = 1 - 1$)								
HNCO($4_{04} \rightarrow 3_{03}$)	28.	81	87.925	3.4	10.55	9.02×10^{-6}	9.2×10^{-12}	9.80×10^{5}
HCN $J = 1 \rightarrow 0$	28.	81	88.632	3.4	4.25	2.41×10^{-5}	1.92×10^{-11}	1.26×10^{6}
HCO+ $J = 1 \rightarrow 0$	28.	81	89.189	3.4	4.28	4.25×10^{-5}	2.3×10^{-10}	1.85×10^{5}
HNC $J = 1 \rightarrow 0$	27.	81	90.664	3.3	4.35	2.69×10^{-5}	8.95×10^{-11}	3.01×10^{5}
HC_3N $J = 10 \rightarrow 9$	27.	81	90.979	3.3	24.01	5.81×10^{-5}	1.1×10^{-10}	5.28×10^{5}
SiO $J = 5 \rightarrow 4$	11.	60	217.105	1.4	31.26	5.20×10^{-4}	1.1×10^{-10}	4.73×10^{6}
$H_2CO(3_{03} \rightarrow 2_{02})$	11.	60	218.222	1.4	21.0	2.82×10^{-4}	1.1×10^{-10}	2.56×10^{6}
$H_2CO(3_{22} \rightarrow 2_{21})$	11.	60	218.476	1.4	68.1	1.57×10^{-4}	5.3×10^{-11}	2.96×10^{6}
$H_2CO(3_{21} \rightarrow 2_{20})$	11.	60	218.760	1.4	68.1	1.58×10^{-4}	4.3×10^{-11}	3.67×10^{6}
$C^{18}O$ $J = 2 \rightarrow 1$	11.	60	219.560	1.4	15.81	6.01×10^{-7}	6.44×10^{-11}	9.33×10^{3}
^{13}CO $J = 2 \rightarrow 1$	11.	60	220.399	1.4	15.87	6.04×10^{-7}	6.44×10^{-11}	9.38×10^{3}
^{12}CO $J = 2 \rightarrow 1$	11.	60	230.538	1.3	16.60	6.91×10^{-7}	6.44×10^{-11}	1.07×10^{4}
^{12}CO $J = 1 \rightarrow 0$	21.	71	115.271	2.6	5.53	7.20×10^{-8}	3.25×10^{-11}	2.22×10^{3}

Notes. The beam sizes (HPBW) and the main beam efficiencies ($\eta_{\rm mb}$) are presented with the rest frequencies ν_0 of the brightest lines in each band and the velocity bin corresponding to 1 MHz. The energy levels $E_{\rm up}$ and Einstein coefficients $A_{\rm ul}$ are based on the Leiden Atomic and Molecular Database (Schöier et al. 2005); the collisional de-excitation rate coefficients $C_{\rm ul}$ are computed at a kinetic temperature of 20 K. The critical density is computed as $n_{\rm c} = A_{\rm ul}/C_{\rm ul}$.

temperature gas, while inside the ring the gas is hotter and not detected at large wavelengths. We extracted different parameters relevant for our study from the work of Viaene et al. (2014) and Draine et al. (2014). These parameters are summarised in Table 2.

Draine et al. (2014) adjusted a physical dust model on *Herschel* and *Spitzer* observations to estimate the mean intensities of starlight heating the dust. These authors computed these mean intensities for the *Herschel*/SPIRE 350 and *Spitzer*/MIPS 160 resolutions of 24.″9 and 39″, respectively. Viaene et al. (2014) account for two more photometric channels. The mean starlight recovered for both resolutions are provided in the second and third columns of Table 2. These differences have an amplitude comparable to the 30% discrepancy between the inferred heating rate and the value predicted by a simple model of bulge starlight discussed by Draine et al. (2014). This provides an idea of the real uncertainty of these estimates, which smooth the substructures, while the corresponding resolutions (24.″9 and 39″) are comparable and larger than those of our millimetre observations (11″, 21″, and 28″; see Table 3). We then provide the cold dust temperatures computed according to the Draine & Li (2007) model as $T^{\rm cold}_{\rm dust} = T^{1/6}$. In the studied area, Draine et al. (2014) find that the starlight heating intensity is compatible with the stars in the bulge, as found by Groves et al. (2012). Relying on *Herschel* data, as well as GALEX, SDSS, WISE, and *Spitzer*, Viaene et al. (2014) model the spectral energy distribution to extract physical quantities. They estimate cold dust temperatures, which are similar to those derived from Draine et al. (2014), as shown in Table 2. The differences could be accounted for by the different datasets used as well as different modelling, Viaene et al. (2014) directly fit the spectral energy distribution, while Draine et al. (2014) relies on a physical model. Viaene et al. (2014) have also provided a warm dust temperature (labelled "birth cloud" in their paper) larger than in the surrounding regions. This suggests that there are substructures linked to recent star formation, corresponding to (weak) star-forming activity (3–15 $M_\odot$/Myr). We can expect the kinetic temperatures to be equal at most to the dust temperature,

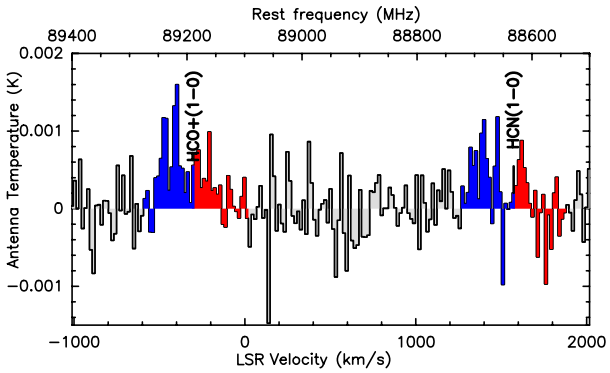

Fig. 2. Averaging of the observations performed in the 88 GHz bandwidth. The main astronomical lines present in the bandwidth are indicated (in black) in the rest-frame frequency of the Andromeda galaxy, whose systemic velocity is around –300 km s^{-1}. For each line, the redshifted and blueshifted parts of the expected velocity range are indicated. The noise level achieved is 0.2 mK for a frequency binning $\Delta\nu$ = 14 MHz. There are clear detections of HCO+(1–0) and HCN(1–0), with possible components at both sides of the systemic velocity.

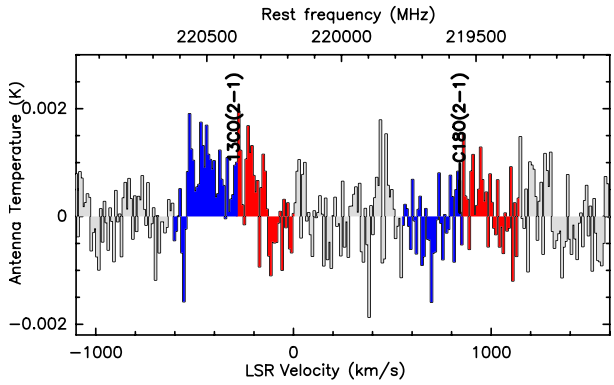

Fig. 3. Averaging of the observations performed in the 216 GHz bandwidth. The ^{13}CO(2–1) and C^{18}O(2–1) lines present in this bandwidth are indicated in the rest-frame frequency of the Andromeda galaxy. For each line, the redshifted and blueshifted parts of the expected velocity range are indicated. The noise level achieved is 3 mK for a frequency binning $\Delta\nu$ = 7 MHz (Δv = 9.5 km s^{-1}). Apart from the multiple-component ^{13}CO(2–1) signal, the C^{18}O(2–1) signal is weak in the receding part of the spectra.

depending on the molecular hydrogen density. In the following, we consider a kinetic temperature of 20 K, which corresponds to the cold gas temperature.

3. Data reduction

We used the CLASS[1] package for the data reduction. We inspected individual spectra. Various interference lines are present far from the expected astronomical signals. These interference lines affect the determination of the baselines, and they have been carefully removed on each spectra. The M31I position has suffered an interference next to the strongest peak of the ^{13}CO(1–0) line. This interference only affects the data acquired on 20th December 2011 (18/30). We thus set to zero the corresponding channels on data taken with the FTS backend with the best spectral resolution (0.26 km s^{-1}).

The observations averaged in the two main bandwidths are presented in the Figs. 2 and 3. We used default weighting with exposure time and system temperature. These spectra reveal multicomponent signals corresponding to the Andromeda velocity range (given its systemic velocity of −300 km s^{-1}).

Characteristics of the main astronomical molecular lines (Schöier et al. 2005) present in the observed bandwidths are provided in Table 3 as follows: half power beam width (HPBW), beam efficiency, rest-frame frequency, and velocity bin corresponding to 14 MHz. We also provide the following characteristics of these molecules: energy level, Einstein coefficient $A_{\rm uk}$, collisional de-excitation rate $C_{\rm ul}$, and critical density $n_{\rm c}$ computed at 20 K. If we consider a collisional temperature of 50 K, the critical densities of HCN and HCO+ increase by 56% and 21%, respectively, but by 7.4% for CO. As indicated in Figs. 2 and 3, there are obvious detections of HCO+(1–0), HCN(1–0), and ^{13}CO(2–1) in the summed spectra and a weak signal in C^{18}O(2–1). There is no obvious contamination from the Milky Way, which could be possible as M31 is 20 deg below the Galactic plane. The spectra obtained in the lower outer bands are presented in Fig. A.1 but do not exhibit any signal. They are used to derived upper limits. For each position, the detections are adjusted with a Gaussian function. Up to three different CO lines are detected at different central velocity at each position. As discussed in Melchior & Combes (2011), this is due to several intervening molecular components along the line of sight.

All of the measurements are summarised in Table A.1. The columns on the top provide the CO line measurements. We provide, for each CO line, the central LSR velocity, the FWHM velocity dispersion Δv, the peak (main-beam) temperature $T_{\rm peak}$, and the integral $I_{\rm CO}$ of the line. In the last two columns, the ^{12}CO/^{13}CO(2–1) and ^{12}CO/C^{18}O(2–1) line ratios and lower limits are shown. We also provide (in the bottom of this table) our ^{12}CO(1–0) measurements described in Melchior & Combes (2011) for M31-I with a beam resolution of 21 arcsec, similar to the resolution achieved for HCN(1–0) and HCO+(1–0), and the $N_{\rm H_2}$ column density derived as discussed below but directly computed from ^{12}CO(1–0). These column density estimates differ by up to a factor of 3 with respect to ^{12}CO(2–1)-based estimates, due to the difference in resolution and corresponding dilution effects.

The columns on the bottom of Table A.1 list HCN(1–0) and HCO+(1–0) measurements and 3σ upper limits (for Δv = 32 km s^{-1}) for some of the lines presented in Table 3. The central table provides the remaining upper limits, as well as column densities (and upper limits) of the species with some detections, namely ^{13}CO, C^{18}O, HCN, and HCO+, assuming local thermal equilibrium (LTE) and optically thin conditions. The column densities have been corrected for the beam filling factor, as further discussed in the next section. Given the velocity dispersion of the observed HCN lines (>25 km s^{-1}), the HCN hyperfine line structure (∼10 km s^{-1}) will not be detected. We also provide the $N_{\rm H_2}$ column densities of molecular hydrogen relying on $X_{\rm CO}$ and CO(2–1)/(1–0) line ratio values. We assume a Galactic ratio $X_{\rm CO} = N_{\rm H_2}/I'_{\rm CO} = 2. \times 10^{20}$ cm^{-2} (K km s^{-1})$^{-1}$ following Strong et al. (1988) and Dame et al. (2001), which is compatible with the findings of Smith et al. (2012) for Andromeda and Mauersberger et al. (2003) for local galaxies. As further discussed in Sect. 4.3, we take $I'_{\rm CO} = I_{\rm CO}/\eta_{\rm bf}$. We assume a CO(2–1)/(1–0) line ratio of 0.8, as measured by Melchior & Combes (2011) in a clump located within 10″ of M31I (and named M31G), to compute $N_{\rm H_2}$ column densities.

[1] Continuum and Line Analysis Single-dish Software, http://www.iram.fr/IRAMFR/GILDAS

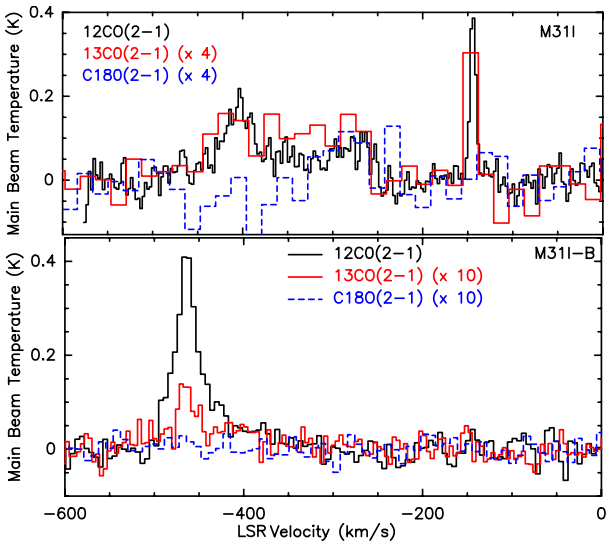

Fig. 4. Carbon monoxide spectra observed on the north-west side of the inner ring are superimposed in velocity. The main beam temperature is provided for ^{12}CO, while the ^{13}CO and C^{18}O spectra are multiplied by a factor of 10 and 4 in the *bottom and top panels*, respectively.

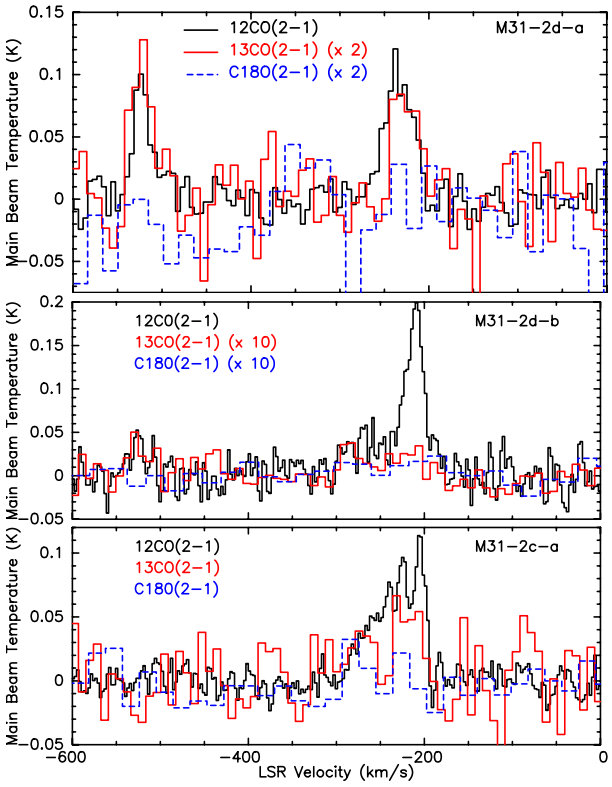

Fig. 5. Carbon monoxide spectra observed on the south-east side of the inner ring are superimposed in velocity. The main beam temperature is provided for ^{12}CO, while the ^{13}CO and C^{18}O spectra are multiplied by a factor of 2, 10, and 1 for the *top, middle, and bottom panels*.

4. Results

In this section, we describe our results. In Sect. 4.1, we describe the detections of five different molecular emission lines in the two observed positions along the minor axis. In Sect. 4.2, we compute the line ratios relying on previous detections and compare them with previous results achieved in other galaxies, in particular, Galactic giant clouds and in M31's disc. In Sect. 4.3, we discuss the basic properties we can derive from the detections, including excitation temperatures, optical depths, beam filling factors, and column densities, and the uncertainties and limitations of this type of analysis. In Sect. 4.4, we discuss the parameters estimated under LTE conditions and compare them with Galactic values. In Sect. 4.5, we run RADEX (van der Tak et al. 2007) simulations to relax the LTE conditions and test the validity of our previous assumptions. While CO emission lines correspond to gas in thermal equilibrium, gas traced by HCN and HCO+ emission lines is under subthermal excitation conditions.

4.1. Description of the detections

The CO lines detected in the north-west (south-east) region are shown in Fig. 4 (Fig. 5). The HCN(1–0) and HCO+(1–0) lines detected on the north-west side are shown in Fig. 6. As shown in Table A.1, we detected up to five different molecular lines (two to four per position and per velocity component). For some positions (M31I, M31I-B, M31-2d-a), there are clearly several well-identified peaks with different velocities, while for other positions the signal is very wide and best fitted with several components. The most striking cases are M31-2c-a, and the low-velocity component of M31-2d-b. The 4σ ^{13}CO(2–1) signal measured for M31-2c-a is affected by a small integration time and the detection integrates several ^{12}CO(2−1) components. Hence, this signal is not used for subsequent stacking. Apart from the ^{12}CO and some ^{13}CO lines, the detections are weak with peak temperatures at the mK level. We detected HCO+(1–0) (HCN(1–0)) at the 6σ and 9σ (4σ and 5σ) levels, while most CO(2–1) detections are above 4σ with a strong one at 11σ; but three weak ^{13}CO detections in the south-east region

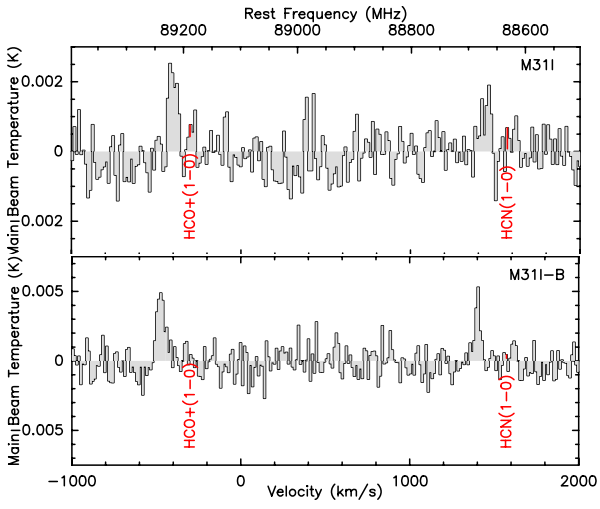

Fig. 6. Signal detected in HCO+(1–0) and HCN(1–0) at the position of M31I (*top*) and M31I-B (*bottom*). The main-beam temperatures are displayed as a function of the rest-frame frequency of the Andromeda galaxy (corresponding to −300 km s^{-1}).

are kept at the 3.3σ level. Knowing the low intensities of these lines, we can infer that it is extremely challenging to perform multi-transition observations of these molecules.

While ^{12}CO and ^{13}CO are detected on both regions, C^{18}O, HCN(1–0) and HCO+(1–0) are only detected on the north-west side. If the dust-to-gas mass ratio is similar on both sides, according to Viaene et al. (2014) we expect a gas mass a factor of 3 larger on this side (see Table 2). Similarly, when one averages the observed column densities of molecular hydrogen

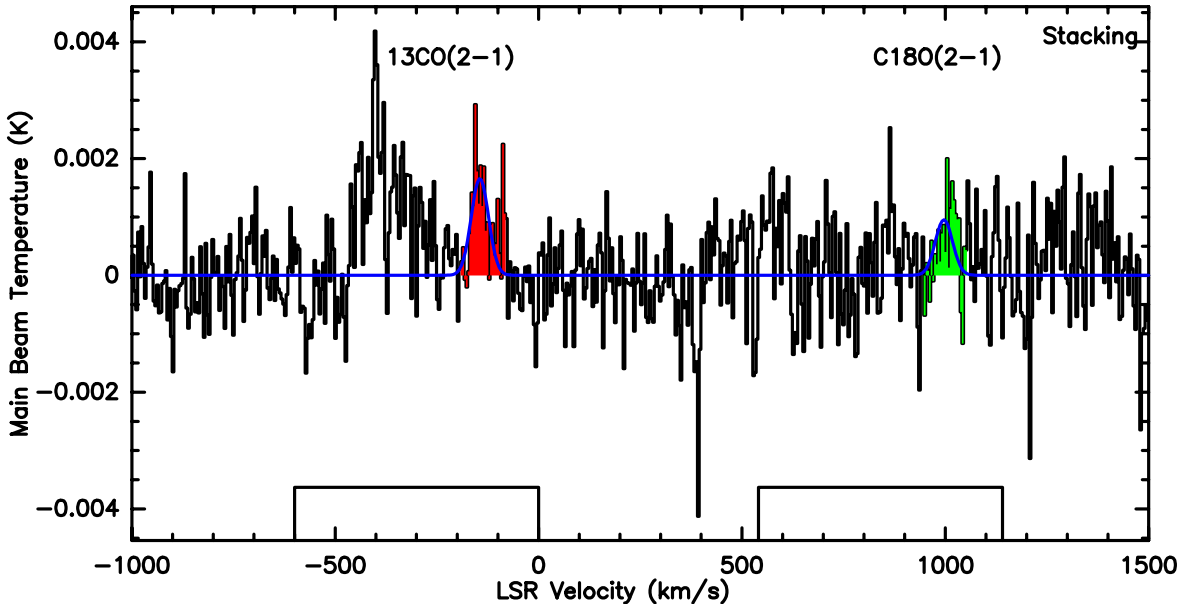

Fig. 7. Stacking centred at −144.3 km s^{-1} of each ^{13}CO(2–1) velocity component with $v > -300$ km s^{-1}. The ^{13}CO component is displayed in red (at −144 km s^{-1}). There is a component (displayed in green at −1285 km s^{-1}) in C^{18}O which appears at the same velocity. The lines adjustment are displayed in blue. The velocity ranges corresponding to the two lines are displayed as rectangles. Standard weights ($\propto T_{\rm int}\,\delta v/{T_{\rm sys}}^2$) for each observation have been used for the averaging.

Table 4. Line measurements for the stacking detection shown in Fig. 7, based on the red ($v > -300$ km s^{-1}) velocities of both regions (excluding the M31-I (3) detection and M31-2c-a(1) tentative ^{13}CO(2–1) detection).

Pos.	$V_{\rm Stack}$	$\langle V_0\rangle$ (km s^{-1})		Δv (km s^{-1})		$T_{\rm Peak}$ (mK)		$I_{\rm line}$ (K km s^{-1})	
		^{13}CO (2–1)	C^{18}O (2–1)	^{13}CO (2–1)	C^{18}O (2–1)	^{13}CO (2–1)	C^{18}O (2–1)	^{13}CO (2–1)	C^{18}O (2–1)
Stack (red)	–144.2	–212	–212	50*	50*	1.65	0.95	0.088 ± 0.015	0.051 ± 0.015
				31				*0.15 ± 0.03*	
SE stack (red)	–226.	–218.	–218.	39*	39*	2.26	1.28	0.094 ± 0.015	0.053 ± 0.015
				39				*0.14 ± 0.04*	
Pos.	$V_{\rm Stack}$	$\langle V_0\rangle$ (km s^{-1})		Δv (km s^{-1})		$T_{\rm Peak}$ (mK)		$I_{\rm line}$ (K km s^{-1})	
		HCO+ (1–0)	HCN (1–0)	HCO+ (1–0)	HCN (1–0)	HCO+ (1–0)	HCN (1–0)	HCO+ (1–0)	HCN (1–0)
SE Stack (blue)	–523	–	–524.5	89*	89 ± 25	–	1.17	<0.075	0.11 ± 0.03
SE Stack (red)	–234	–231	–231	78 ± 29	78*	0.74	0.85	0.061 ± 0.026	0.070 ± 0.024

Notes. We present the central velocities, velocity dispersions, peak temperatures, and integrated lines. $\langle V_0\rangle$ is the averaged velocity of the spectra used for each stacking. Similar stacking based on the ^{12}CO(2–1) velocities is performed for HCN and HCO+ spectra of the south-east (SE) positions. As shown in Fig. A.2, redshifted (blueshifted) velocities are considered separately.

provided in Table A.1 along the two lines of sight, the north-west positions have a column density a factor of 2 higher than the south-east positions. Also, the radiation field (U) is larger on the south-east side than in the north-west side: this may be related to larger CO column densities and to the fact that dense gas (C^{18}O, HCN, HCO+) is not directly detected in the south-east positions.

The C^{18}O detection corresponds to the component at the systemic velocity, while the HCN and HCO+ detections are in the blueshifted components. However, as shown in Fig. 7, stacking of the $v > -300$ km s^{-1} ^{13}CO detections (excluding the M31-I(3) detection) also reveals a redshifted component in C^{18}O with an amplitude comparable with ^{13}CO. The characteristics of this stacking detection is presented in Table 4. We thus have at least two different C^{18}O components in two different velocity ranges.

Figure A.2 denotes the stacking of $v < -300$ km s^{-1} and $v > -300$ km s^{-1} of HCN(1–0) and HCO+(1–0) spectra. The detected signals are summarised in Table 4. The south-east spectra have been shifted to the ^{12}CO velocities and averaged with standard weights ($\propto T_{\rm int}\,\delta v/{T_{\rm sys}}^2$). For HCN, there is 3.7$\sigma$ detection in the blue stacking while there is a possible 2.6σ detection in the red stacking. In contrast to the direct observations, the stacked HCN signal is stronger than the HCO+ signal, with a HCO+/HCN line ratio of 0.87 ± 0.49 in the red stacking and <0.68 in the blue stacking.

The difficulty of the interpretation of these dense gas detections is due to a complicated configuration. We integrate the signal over a relatively large beam (42–106 pc in projection), and the velocity dispersions are significantly larger than those (~2 km s^{-1}) detected in M31's main disc (Schruba et al., in prep.)

Table 5. Observed line ratios.

Position	V_0 (km s^{-1})	HCO+/HCN (1–0)	HNC/HCN (1–0)	HOC+/HCO+ (1–0)	^{12}CO/HCO+ (1–0)	^{12}CO/HCN (1–0)	^{12}CO/^{13}CO (2–1)
I(2)	∼−402	1.5 ± 0.5	<1.09	<0.59	43. ± 8	62. ± 18	24. ± 5
I-B(1)	∼−470	1.7 ± 0.4	<0.35	<0.21	*53. ± 7*	*89. ± 18*	30. ± 3
Position	V_0 (km s^{-1})	HCO+/HCN (1–0)	^{12}CO/C^{18}O (2–1)	^{13}CO /C^{18}O (2–1)			^{12}CO/^{13}CO (2–1)
I(3)	∼−291		28.6 ± 9.5	1.48 ± 0.51			19.4 ± 5.0
Stack (red)			*30 ± 12*	1.73 ± 0.59			*17.4 ± 4.1*
SE stack (red)		0.87 ± 0.49	*33 ± 14*	1.77 ± 0.58			*18.7 ± 5.1*

Notes. These ratio are computed with the velocity-integrated intensities measured within similar beams for the same component. Numbers in italics correspond to tentative estimates: ^{12}CO(1–0) are derived from ^{12}CO(2–1) with a 0.8 line ratio, stacked ^{12}CO(2–1) and ^{13}CO(2–1) are computed as the sum of the detected lines; and ^{13}CO(2–1) and C^{18}O(2–1) are measured on stacked spectra.

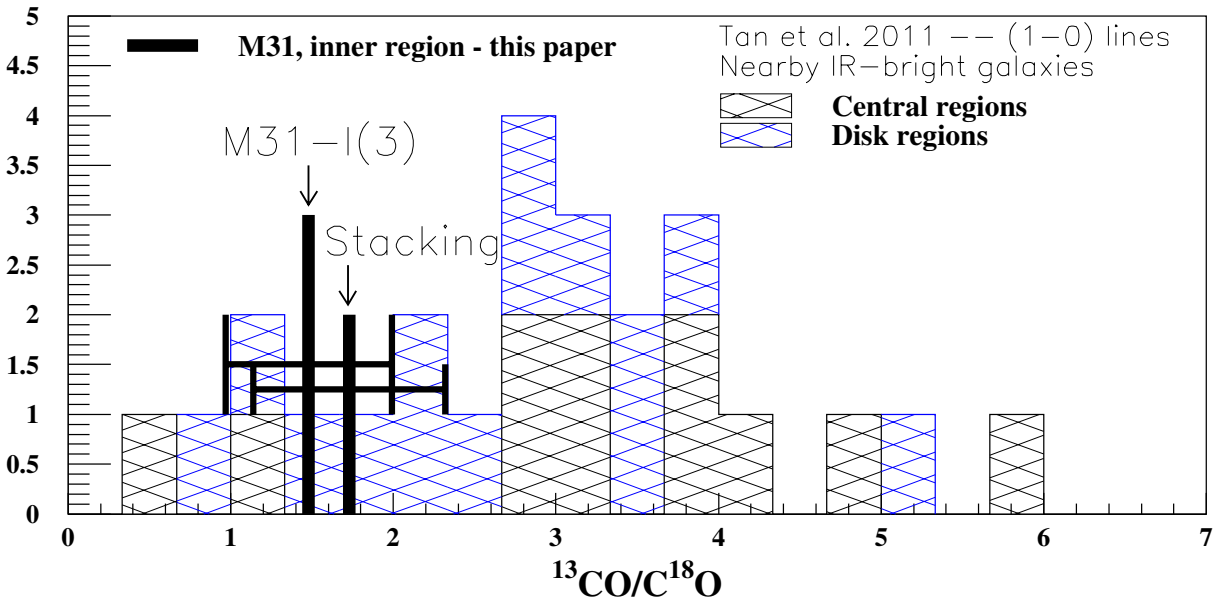

Fig. 8. Comparison of our ^{13}CO/C^{18}O(2–1) line ratio measurements (M31-I(3) and stacking) corresponding to different clouds (i.e. with different velocities) with previous measurements in nearby galaxies from Tan et al. (2011). The hatched histogram displayed the original ^{13}CO/C^{18}O(1–0) line ratio.

with $\Delta v > 30$ km s^{-1} for most of our detections. This is because of the strong velocity gradient present in this region and to the superposition of several clouds. This also points towards inner elongated orbits observed with a large radial velocity range (in contrast to the outer orbits observed in the main disc where small velocity dispersions (∼2 km s^{-1}) are expected and observed). M31-I(1) has a smaller velocity dispersion, which is still four times larger than disc clouds. The other components of M31-I are very large and could correspond to an underlying (possibly continuous) component with a 150 km s^{-1} width with non-circular orbits. This could be a relic of a spiral arm or dissolved bar.

4.2. Observed line ratios

In this section, we analyse the observed line ratios, which are directly derived from the observations.

When one computes line ratios based on velocity-integrated intensities as shown in Table 5, dilution effects due to the unknown beam filling factors should be removed at least at first order. Empirical comparisons with similar targets can be performed.

Figure 8 shows that our measured ^{13}CO/C^{18}O(2–1) line ratios lie below the (1–0) measurements of Liu et al. (2014) in infrared Galactic dark clouds (average 4.4 ± 1.3; see their Fig. 2), but corresponds to the lower end of the Tan et al. (2011) starburst sample distribution based on ^{13}CO/C^{18}O(1–0) line ratio. Our measured line ratios are also significantly lower than the M51's spiral arms gas detected by Schinnerer et al. (2010; their average ^{13}CO/C^{18}O line ratio: 3.5).

It is remarkable that the C^{18}O detection is at a level comparable to the ^{13}CO detection, in contrast to what is observed in the Galaxy (e.g. Nishimura et al. 2015; Shimajiri et al. 2014), where the C^{18}O is usually 10 to 150 times weaker than ^{13} CO. ^{13}CO/C^{18}O line ratios close to one are expected if ^{13}CO is optically thick or if ^{13}C is depleted with respect to ^{12}C, such as after a starburst.

In Fig. 9, we compare our ^{12}CO/^{13}CO(2–1) line ratios with values measured previously in other galaxies. We consider the following catalogues:

– the (2–1) line ratio compilations for different morphological types from Krips et al. (2010; we provide the different morphological types under the form of hatched histogram);

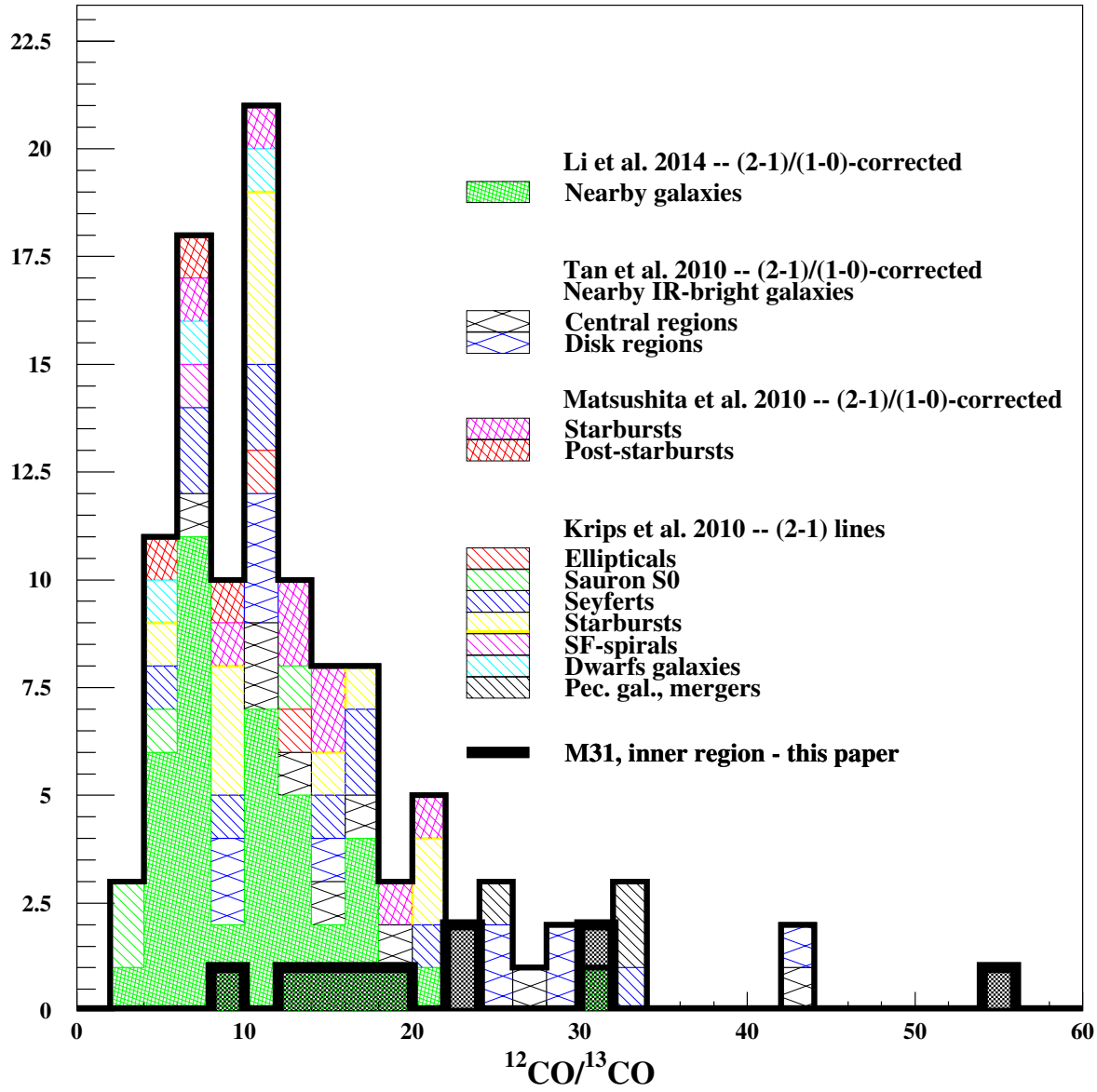

Fig. 9. Comparison of our $^{12}CO/^{13}CO$ line ratio with previous measurements in nearby galaxies. The hatched histogram displayed the $^{12}CO/^{13}CO$ line ratios with available morphological types. The Li et al. (2011), Matsushita et al. (2010) and Tan et al. (2011) samples measured the (1–0) transition and have been corrected by a factor 1.33 as discussed in the text. The Krips et al. (2010) sample and our measurements were directly measured the (2–1) transition. The black full line histogram gathers all the four samples corrected to (2–1). The black thick line histogram in the bottom corresponds to the measurements performed in this paper. The average $^{12}CO/^{13}CO$ detected in this paper tends to be a bit larger than the main distribution from other areas and other galaxies (but well below the standard isotopic ratio of 53 Wilson & Rood 1994). The largest value above 50 might corresponds to an optically thin cloud, but it is affected by a large error bar (30%, see Table A.1).

- the (1–0) line ratio measured by Li et al. (2015) in nearby galaxies;
- the (1–0) line ratio measured by Matsushita et al. (2010) in starburst and post-starburst galaxies; and
- the (1–0) line ratio measured by Tan et al. (2011) in nearby infrared-bright galaxies and starbursts.

The (1–0) line ratios have been corrected with the average $^{12}CO/^{13}CO(1–0)/(2–1)$ ratio (1.33) from Krips et al. (2010). These authors found that the $^{13}CO/^{12}CO(2–1)$ ratios of three SAURON galaxies are somewhat higher than those in galaxies of different Hubble types. The hatched histogram of Fig. 9 shows the different morphological types when available, and indicates that there is no trend with morphology. As discussed by Li et al. (2015), the isotopologue ratio does not depend on the morphological type of the galaxy. Our measurements (with an average $^{12}CO/^{13}CO = 20$), shown with a thick line hatched histogram, lie below the standard isotopic ratio (53) (Wilson & Rood 1994) but fall in the same range as the other measurements. This is consistent with the fact that ^{12}CO is optically thick. As a result of very different cloud geometries, it is difficult to compare our $^{13}CO/^{12}CO(2–1)$ line ratio measurements in M31 with studies performed in Galactic regions. For instance, Orion regions observed by Nishimura et al. (2015) or *Planck* cold dust clumps (Wu et al. 2012) exhibits relatively low $^{12}CO/^{13}CO$ line ratio (~2–3) because the dense clouds fill the beam and ^{12}CO is very optically thick.

Figure 10 shows the HCN/HCO+(1–0) and $^{13}CO/^{12}CO(2–1)$ ratios we measured in the components approaching us in the north-western positions and the south-east stacking

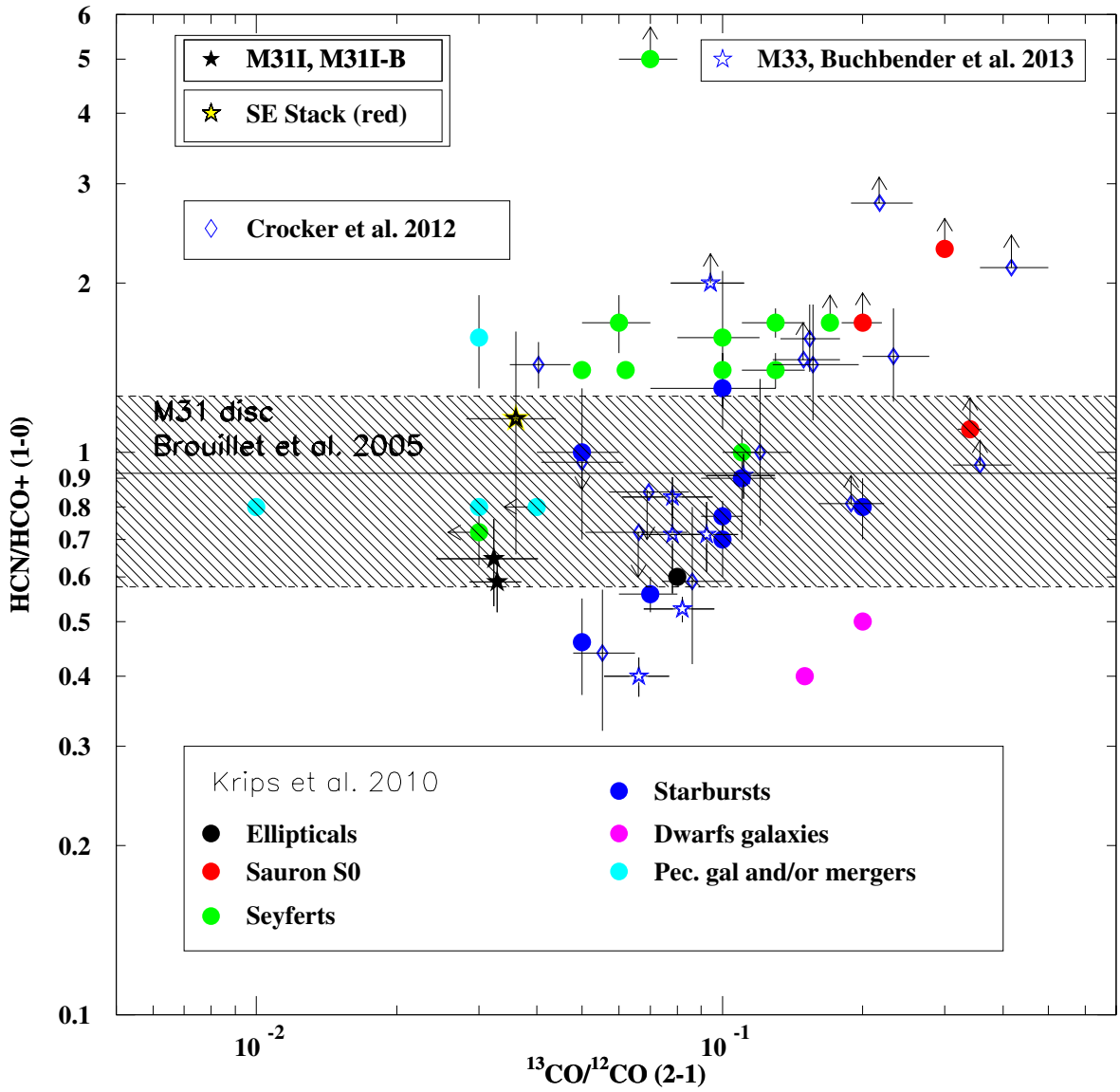

Fig. 10. Comparison with other catalogues (1). HCN/HCO+(1–0) line ratio versus ^{13}CO/^{12}CO(2–1) line ratio. The two north-west detections presented in this paper (M31I and M31I-B) together with the red south-east stacking measurement are superimposed on previous measurements, namely: a compilation of various types of galaxies from Krips et al. (2010), early-type galaxies from Crocker et al. (2012) and M33's giant molecular clouds from Buchbender et al. (2013). The hatched area corresponds to the mean HCN/HCO+(1–0) line ratio obtained by Brouillet et al. (2005) in M31's disc. Surprisingly, our detections, compatible with the M31 disc measurements of Brouillet et al. (2005), lie in "the peculiar/merger region".

detection, which is redshifted. We compare these line ratios with previous observations from the literature. By superposing our measurements on the wide range of galaxy types observed by Krips et al. (2010), we find that our detections seem to lie in the peculiar/merger region, rather than in the star-forming (M33) and starburst part of the diagram. The HCN/HCO+ line ratio is compatible with the average ratio computed for M31's disc by Brouillet et al. (2005). Again, the Galactic clouds of Nishimura et al. (2015) lie on the right hand side of this figure and are difficult to compare with M31 measurements. Our measurements are not compatible with Seyfert galaxies, which makes sense because there is no sign of active galactic nuclei (AGN) in M31 (Li et al. 2011). Interestingly, on the one hand, the HCN/HCO+ line ratio detected here is compatible with the value (1.5) measured by Liu et al. (2013) in infrared dark clouds. The red stacking ratio has a larger value but it is affected by a large error bar. On the other hand, HCN/HNC(1–0) line ratio is systematically larger than that measured in dark clouds by these authors. The HCN(1–0) line detections enable us to estimate lower limits on the HCN/HNC(1–0) line ratio towards the positions in the north-western area (M31I and M31I-B), which are 0.9 and 2.9, respectively. Figure A.3 compares the HCO+/CO(1–0) and HCN/CO(1–0) line ratios detected on the north-western side of the inner ring with other positions in M31's main disc (Brouillet et al. 2005) and with other galaxies. Our detections are compatible with the Brouillet et al. (2005) measurements performed in M31's disc, but lie in the lower end of the overall distribution of Krips et al. (2010). Figure A.4 shows the detections and the upper limits of our observed CO line ratios.

Our detections differ from measurements performed in M33's giant molecular clouds (Buchbender et al. 2013). They are compatible with line ratios available for clouds in M31's disc studied by Brouillet et al. (2005), but there is no information

on the CO isotopic ratio in the disc. The main trends regard the ^{13}CO/C^{18}O line ratio, which is depleted, while the HCN/HCO+(1–0) line ratio is very typical of what is observed in other local galaxies. Liu et al. (2013) have studied infrared dark clouds and argue that the abundance ratio of HCN and HCO+ may be unaffected by the environment. Even though the 100 μm and A_B maps shown in Fig. 1 do not exhibit strong features, we argue in Sect. 4.3 that our detections correspond to dense cores. These ratios depend non-linearly on physical parameters, such as optical depth, excitation temperature, density, and some lines are probably optically thick and not necessarily in thermal equilibrium. This is explored further in Sects. 4.3–4.5.

4.3. Estimate of the beam filling factors

The temperatures we have detected for ^{12}CO(2–1) are well below the cosmological background, even though the molecular lines are detected in emission. This is due to the low surface filling factor of the gas detected in the beam. In this section, we try to derive estimates of the beam filling factors affecting our observations. These estimates affect all absolute parameters (temperature, density, abundance, column density, etc.) that could be determined later, and thus the possible interpretation of the state of the detected gas.

As the average ^{12}CO/^{13}CO line ratio (20) is well below the standard Galactic ^{12}C/^{13}C abundance ratio (53) of Wilson & Rood (1994) and the C^{18}O line intensity comparable to the ^{13}CO intensity, we consider that the ^{12}CO line is optically thick. As the gas is detected in emission, we can then derive a minimal excitation temperature of about 3 K from the intrinsic brightness temperature T_B, with the usual formula

$$T_B = (f(T_{ex}) - f(T_{bg})) \times (1 - e^{-\tau}) \quad (1)$$

where

$$f(T) = \frac{\frac{h\nu}{k}}{\exp(\frac{h\nu}{kT}) - 1}. \quad (2)$$

Relying on the modelling of infrared measurements, Viaene et al. (2014) and Draine et al. (2014) estimated a cold dust temperature of the order of 20 K (see Table 2). Since we measured the line ratio CO(2–1)/CO(1–0) ~ 0.8 (Melchior & Combes 2011), which is relatively high, we assume that the line is thermalised and that we can define a single excitation temperature. This makes sense for cold gas in the central part of a large galaxy. Most importantly, one has to take into account the beam filling factor η_{bf}, which is linked to the intrinsic brightness temperature as follows:

$$T_B = T_{peak}/\eta_{bf} \quad (3)$$

where T_{peak} is the peak temperature measured for our detections, i.e. the observed diluted main beam temperature. Given our assumptions about the excitation temperature and the ^{12}CO optical depth, we can derive η_{bf} from our ^{12}CO(2–1) detections as

$$\eta_{bf} = T_{peak} / \left[f(T_{ex}) - f(T_{bg}) \right]. \quad (4)$$

If the molecular lines are close to thermal equilibrium around 20 K, the beam filling factor is below one percent. This order of magnitude is consistent with several different qualitative arguments, as follows: (1) the beam size is 44 pc for ^{12}CO(2–1), while typical interstellar filaments have a size of 0.1 pc (André et al. 2014). (2) We are detecting gas complexes, which are probably extended and patchy according to the optical image. (3) The large velocity dispersions also suggest that we are integrating gas along a large depth. (4) Last, if one considers a standard gas-to-dust relation $N_H = 0.94 \times 10^{21} \times A_V$ cm^{-2} (Bohlin et al. 1978), we estimate A_V = 2.6 and 1.4 for M31-I(2) and M31-IB(1) (with no beam-filling factor corrections), while lower limits on extinction estimated on the optical images are of the order of A_B = 0.2 (Melchior & Combes 2011). This order of magnitude of the beam filling factor is also compatible with values previously discussed in the literature, for example Carlstrom (1988) estimated a volume filling factor smaller than 10^{-3} in M82, while Berkhuijsen & Fletcher (2015) estimate a filling factor of approximately 4% in M31 and M51.

In the following, we consider that ^{12}CO(2–1) is optically thick to determine the beam filling factors at thermal equilibrium, as provided in Table 6. The values we estimate for η_{bf} are consistent with Ginsburg et al. (2011), who discuss that giant molecular clouds consist of very low volume-filling factor (~5×10^{-3}) high-density ($n(H_2) \sim 3 \times 10^4$ cm^{-3}) clumps, as well as typical starburst galaxies (with $\eta_{bf} < 0.01$).

For a given excitation temperature, we can derive the optical depth corresponding to each optically thin line:

$$\tau_{mol} = -\ln\left(1 - \frac{T_{peak}}{\eta_{bf}} \frac{1}{f(T_{ex}) - f(T_{bg})}\right). \quad (5)$$

We can then compute the column density associated to each molecular line assuming an excitation temperature T_{ex}:

$$N_{mol} = \frac{8\pi k}{hc^3} \frac{Q(T)}{g} e^{E_{up}/T_{ex}} \frac{\tau_{mol}}{1 - e^{-\tau_{mol}}} \frac{\nu^2 I_{CO}}{\eta_{bf}} \quad (6)$$

where g is the level degeneracy g = 5 for CO(2–1) molecules and g = 3 for HCN(1–0) and HCO+(1–0), $Q(T)$ is the rotational partition function and E_{up} is the energy level provided in Table 3. We also consider the beam filling factors defined in Table 6. The factor $\frac{\tau_{mol}}{1-e^{-\tau_{mol}}}$ enables to account for non-optically thin conditions (e.g. Mangum & Shirley 2015). However, in practice, we have to assume an unknown abundance ratio to determine τ_{mol} if it is optically thick, which limits the use of corrected column density in this analysis.

The optical depths thus computed and provided in Table 6 show that our hypotheses are consistent: ^{13}CO is optically thin. In Sect. 4.4, we discuss abundances estimated assuming LTE conditions. In Sect. 4.5, we explore how to derive molecular hydrogen densities for lower excitation temperatures with RADEX simulations (van der Tak et al. 2007).

4.4. Local thermal equilibrium conditions

We consider here that the different detected lines correspond to some gas in LTE with an excitation temperature of 20 K. This enables us to derive physical parameters from the observations with an analytical formula and to give an initial idea of the physical configurations of the observed complexes.

4.4.1. Optical depths and column densities

With these assumptions, we derived optical depths for ^{13}CO(2–1), C^{18}O(2–1), HCO+(1–0) and HCN(1–0) with the filling factor η_{bf}(20 K), computed in Sect. 4.3. These lines are optically thin, as shown in Table 6.

If we consider standard ^{12}CO/^{13}CO line ratios from Wilson & Rood (1994) of 53 for the molecular ring (20 for the Galactic centre) and the ^{13}CO optical depths provided in Table 6, we

Table 6. Estimate the beam filling factor $\eta_{bf}(T_{ex})$ for different excitation temperatures, assuming that the ^{12}CO(2–1) line is optically thick.

Positions	η_{bf}(25 K)	η_{bf}(20 K)	η_{bf}(15 K)	η_{bf}(10 K)	η_{bf}(5 K)	$\tau_{^{13}CO}$	$\tau_{C^{18}O}$	τ_{HCO+}	τ_{HCN}	$\tau^{MR}_{^{12}CO}$	$\tau^{GC}_{^{12}CO}$
I(1)	2.1×10^{-2}	2.9×10^{-2}	4.2×10^{-2}	8.0×10^{-2}	3.6×10^{-1}	0.049				2.57	0.97
I(2)	7.4×10^{-3}	9.9×10^{-3}	1.5×10^{-2}	2.8×10^{-2}	1.2×10^{-1}	0.033		0.021	0.012	1.77	0.67
I(3)	3.9×10^{-3}	5.2×10^{-3}	7.7×10^{-3}	1.5×10^{-2}	6.6×10^{-2}	0.056	0.038			2.97	1.12
I-B(1)	1.8×10^{-2}	2.4×10^{-2}	3.6×10^{-2}	6.7×10^{-2}	3.0×10^{-1}	0.033		0.016	0.016	1.74	0.66
I-B(2)	2.5×10^{-3}	3.3×10^{-3}	4.9×10^{-3}	9.3×10^{-3}	4.2×10^{-2}	0.089				4.73	1.78
2d-a(1)	5.1×10^{-3}	6.7×10^{-3}	1.0×10^{-2}	1.9×10^{-2}	8.5×10^{-2}	0.059				3.12	1.18
2d-a(2)	5.3×10^{-3}	7.1×10^{-3}	1.1×10^{-2}	2.0×10^{-2}	9.0×10^{-2}	0.051				2.69	1.02
2d-b(1)	8.9×10^{-3}	1.2×10^{-2}	1.8×10^{-2}	3.3×10^{-2}	1.5×10^{-1}	0.018				0.97	0.37
2d-b(2)	2.2×10^{-3}	3.0×10^{-3}	4.4×10^{-3}	8.3×10^{-3}	3.8×10^{-2}	0.063				3.36	1.27
2d-b(3)	1.9×10^{-3}	2.6×10^{-3}	3.8×10^{-3}	7.2×10^{-3}	3.2×10^{-2}	0.135				7.16	2.70
2c-a(1)	3.1×10^{-3}	4.1×10^{-3}	6.1×10^{-3}	1.2×10^{-2}	5.2×10^{-2}	0.071				3.78	1.43
2c-a(2)	2.7×10^{-3}	3.7×10^{-3}	5.4×10^{-3}	1.0×10^{-2}	4.6×10^{-2}						
2c-a(3)	5.0×10^{-3}	6.6×10^{-3}	9.8×10^{-3}	1.9×10^{-2}	8.4×10^{-2}						

Notes. The next four columns provide the optical depths for ^{13}CO(2–1), C^{18}O(2–1), HCO+(1–0), and HCN(1–0) assuming an excitation temperature of 20 K and a beam filling factor equal to that derived from ^{12}CO, i.e. η_{bf}(20 K). The next two columns provide the ^{12}CO(2–1) column densities computed for two standard ^{12}CO/^{13}CO line ratios for the molecular ring (MR) and Galactic centre (GC) from Wilson & Rood (1994).

Table 7. Abundance ratios.

	Measured values (LTE)				Galactic values			
	I(3)		Red Stacking					
Transition (2–1)	X^{Obs}	^{13}CO /Mol	X^{Obs}	^{13}CO /Mol	X^{GISM} (MR)	X^{GISM} (GC)	^{13}CO /Mol (MR)	^{13}CO /Mol (GC)
^{13}CO	$10.8 \pm 2.7 \times 10^{-8}$	1	*8.0 ± 1.5* $\times 10^{-8}$	1	5.3×10^{-7}	1.4×10^{-6}	1	1
C^{18}O	$7.3 \pm 2.4 \times 10^{-8}$	1.48 ± 0.51	*4.6 ± 1.4* $\times 10^{-8}$	1.73 ± 0.58	8.6×10^{-8}	1.1×10^{-7}	6.2	12.7
	Measured values (LTE)				Galactic values			
	I(2)		SE red Stacking					
Transition (1–0)	X^{Obs}	Mol /HCO+	X^{Obs}	Mol /HCO+	X^{GISM}	Mol /HCO+		
HCN	$1.8 \pm 0.3 \times 10^{-10}$	1.11 ± 0.22	*2.6 ± 0.5* $\times 10^{-10}$	1.96 ± 0.64	1.9×10^{-9}	4.0		
HCO+	$1.6 \pm 0.2 \times 10^{-10}$	1	*1.3 ± 0.3* $\times 10^{-10}$	1	4.7×10^{-10}	1		
	I-B(1)							
Transition (1–0)	X^{Obs}	Mol /HCO+						
HCN	*1.3* $\pm 0.2 \times 10^{-10}$	1.01 ± 0.14						
HCO+	*1.3* $\pm 0.1 \times 10^{-10}$	1						

Notes. For each molecule, we provide the expected abundances, assuming LTE and optically thin conditions, to compare them with Galactic values. We provide abundances and abundance ratios for two positions M31-I(3) and M31-I(2) (Cols. 2–3) and the stacking detections (Cols. 4–5), and then compare these values with those expected for the Galactic interstellar medium, at 4 kpc (MR) and at the Galactic centre (GC), derived from Bergin et al. (1995) and Wilson & Rood (1994) (Cols. 6–9). When ^{12}CO(1–0) is not measured directly, the numbers are in italics.

estimate an average optical depth for ^{12}CO of 3.2 (1.2). The ^{12}CO(2–1) transition is indeed optically thick. These different optical depths discussed above are provided for each line of sight in Table 6.

In the middle panel of Table A.1, we provide column densities of our main detections (^{13}CO, C^{18}O, HCN, HCO+), some upper limits for optically thin gas ($\tau \ll 1$) in LTE, and the column density of molecular hydrogen derived empirically from the ^{12}CO line intensity with a X_{CO} factor as discussed in Sect. 3. All column densities account for the beam filling factor η_{bf}.

4.4.2. Abundance ratios

In Table 7, we tentatively compute the abundances (i.e. the ratio of the column density of the molecule with respect to the column density of molecular hydrogen) for the direct and stacking detections. In order to calculate the ratio of lines measured with similar HPBW resolutions, we use ^{12}CO(2–1) to derive the molecular hydrogen column density for the ^{13}CO(2–1) and C^{18}0(2–1) measurements and ^{12}CO(1–0) (available for M31-I) for HCN(1–0) and HCO+(1–0) abundances. We thus study M31I(3) and M31I(2). We also include the red stacking detections for which we adopt an ad-hoc estimate of N_{H_2} based on the averaging of the measured $I_{^{12}CO}$ and $I_{^{13}CO}$ measurements performed with the spectra used for the stacking: a scaling factor is derived from these averaged measurements and applied to the stacked ^{13}CO(2–1) measurement to estimate ^{12}CO(2–1). It is then scaled to ^{12}CO(1–0) with the 0.8 factor, as discussed in Sect. 3. For the sake of discussion, we also provide (in italics) M31I-B(1) and the stacking measurements for which we

have HCN(1–0) and HCO+(1–0) measurements to no direct ^{12}CO(1–0) measurements. As shown in Table 7, the molecular hydrogen column density exhibits variations up to a factor 3 owing to different resolutions (11″ and 21″).

We use the column densities presented in Table A.1 and described in Sect. 3. We also provide for comparison the abundance values for the Galaxy computed in the molecular ring (MR) at 4 kpc from the Galactic centre and in the Galactic centre (GC) by Bergin et al. (1995) and Wilson & Rood (1994).

The abundances are affected by the uncertainties in the molecular hydrogen column densities computed empirically with the X_{CO} factor and by the uncertainties in the excitation temperatures. For the CO transitions, we can expect that variations of the excitation temperatures are a secondary effect, and we can thus rely on abundance ratios for optically thin transitions.

The detected ^{13}CO/C^{18}O abundance ratios are very different from the Galactic values. There is a discrepancy of a factor 4 with the molecular ring (MR), and a factor 9 with respect to the Galactic centre (GC) where gas has been processed regularly. Obviously, the gas is not in the same state as these obvious regions in the Galaxy. Considering the C^{18}O abundances in M31-I(3), it is relatively close to the molecular region value, while the discrepancy affects the ^{13}CO. For the stacking, the C^{18}O abundance is a bit smaller and intermediate between GC and MR values, even though it is compatible with the M31I(3) abundance within 1σ. While the C^{18}O abundance lies in the same range as the Galactic value, the ^{13}CO abundance is deficient.

The HCN and HCO+ abundances differ from the Galactic values, and the abundance ratio. These discrepancies could be due to different excitation temperatures. However, our different measurements are globally compatible within 3σ. Liu et al. (2013) measured an HCN/HCO+(1–0) abundance ratio of 1.2 ± 0.4 in infrared dark clouds (IRDC) and discuss that this ratio may be unaffected by the environment. In parallel, they measured an average HNC/HCN abundance ratio of 1.47 ± 0.50 in IRDC, while the 3σ upper limit we derived on the HNC/HCN abundance ratio for M31I-B(1) and M31I(2) is 1.01 and 1.14. As these authors discuss, we can argue that our detections are different from the IRDC. Our upper limits allow us to put some constraints on the kinetic temperature (e.g. Schilke et al. 1992; Hirota et al. 1998). This corresponds to kinetic temperatures in the range 38–100 K and 14–50 K, and is compatible with the results of Viaene et al. (2014) based on the analysis of infrared data. Similarly, we get HCO+/HOC+ abundance ratios larger than 1.7 and 4.9, but this is not restrictive enough as previous detections are in the range 50–12 500 (Savage & Ziurys 2004).

In the next section, we explore with non-LTE simulations how different excitation temperatures could affect the different parameters and help to get a coherent set of parameters.

4.5. RADEX simulations

In order to check the consistency of our parameters, we ran some simulations with the radiative transfer code RADEX (van der Tak et al. 2007) for several molecules. The idea is to relax the LTE conditions to scan a range of excitation temperatures and of molecular hydrogen densities. Knowing the column densities of each emission line, we can estimate the excitation temperature and the density. As indicated in the figures discussed below, the standard abundances correspond to optically thick conditions and can be excluded.

In Fig. 11, we show the results of the simulations run for HCN and superimpose the various parameters discussed in the previous section, namely, the optical depth and the molecule column densities per unit velocity derived from our observations and from standard abundances. These results support the view that this gas is subthermally excited at 9 K with a density smaller than the critical density, which is provided in Table 3. This critical density plotted here (and in Figs. A.5 and 12) does not match T_{ex} = 20 K, confirming the arguments of Shirley (2015) that this quantity is an oversimplified and incorrect interpretation of the excitation density of a transition. The results of the constraints of RADEX simulations with our observations are also consistent with the HCN(1–0) transition being optically thin. We detected two dense clumps with a molecular hydrogen density $n_{H_2} = 4.8 \times 10^5$ cm^{-3} on the north-west side of the inner ring. Our abundances are more than a factor of 10 lower than the column densities derived from the standard abundances estimated by Bergin et al. (1995) in the molecular ring (MR), and the discrepancy would be even larger if one considers the Galactic centre conditions.

We performed similar computations for HCO+(1–0), as shown in Fig. A.5. We also find subthermal conditions with a molecular hydrogen density smaller than the critical density and an excitation temperature of 9 K. The abundances are also smaller (factor 5–6) than the column densities derived from the standard MR abundances (Bergin et al. 1995). The gas associated with the HCO+(1–0) detection has a density of 1.0 × 10^5 cm^{-3}.

We applied the same procedure to M31-I(3) where ^{13}CO and C^{18}O have been detected, as shown in Fig. 12. On the one hand, the best excitation temperature is consistent with 17 K but we cannot exclude 20 K given the error bars. On the other hand, the simulations support a molecular hydrogen density larger than the critical density. These lines are close to LTE conditions and trace clumps with a density larger than 2.24 × 10^4 cm^{-3}. The ^{13}CO measured abundance is smaller than the standard abundances by a factor 5, while the C^{18}O measured abundance is compatible within the error bars of the standard abundances estimated in the molecular ring.

The abundances we have derived are systematically smaller than the standard abundances (Bergin et al. 1995) for the molecular ring, but for C^{18}O. This is consistent with our previous discussion that ^{12}CO is optically thick and ^{13}CO depleted, with LTE and optically thin conditions for ^{13}CO and C^{18}O. HCN and HCO+ abundances are consistent with subthermal excitation conditions with excitation temperatures of 9 K and are smaller than the standard abundances. As shown in Figs. A.3 and 10, the HCO+/HCN line ratio measured in the clouds studied here is similar to that measured in M31's disc by Brouillet et al. (2005).

5. Discussion

In this section, we discuss our dense gas detection, how it can improve our knowledge of this inner region, and whether the properties of this gas are consistent with our understanding of previous observations. In Sect. 5.1, we discuss the geometrical configuration of the gas: the information derived from dust extinction affecting point sources, and the properties of various gas components observed at different wavelengths. In Sect. 5.2, we discuss our knowledge of the heating sources and the properties of the interstellar medium in this region. In Sect. 5.3, we discuss the kinematical information obtained with our millimetre observations.

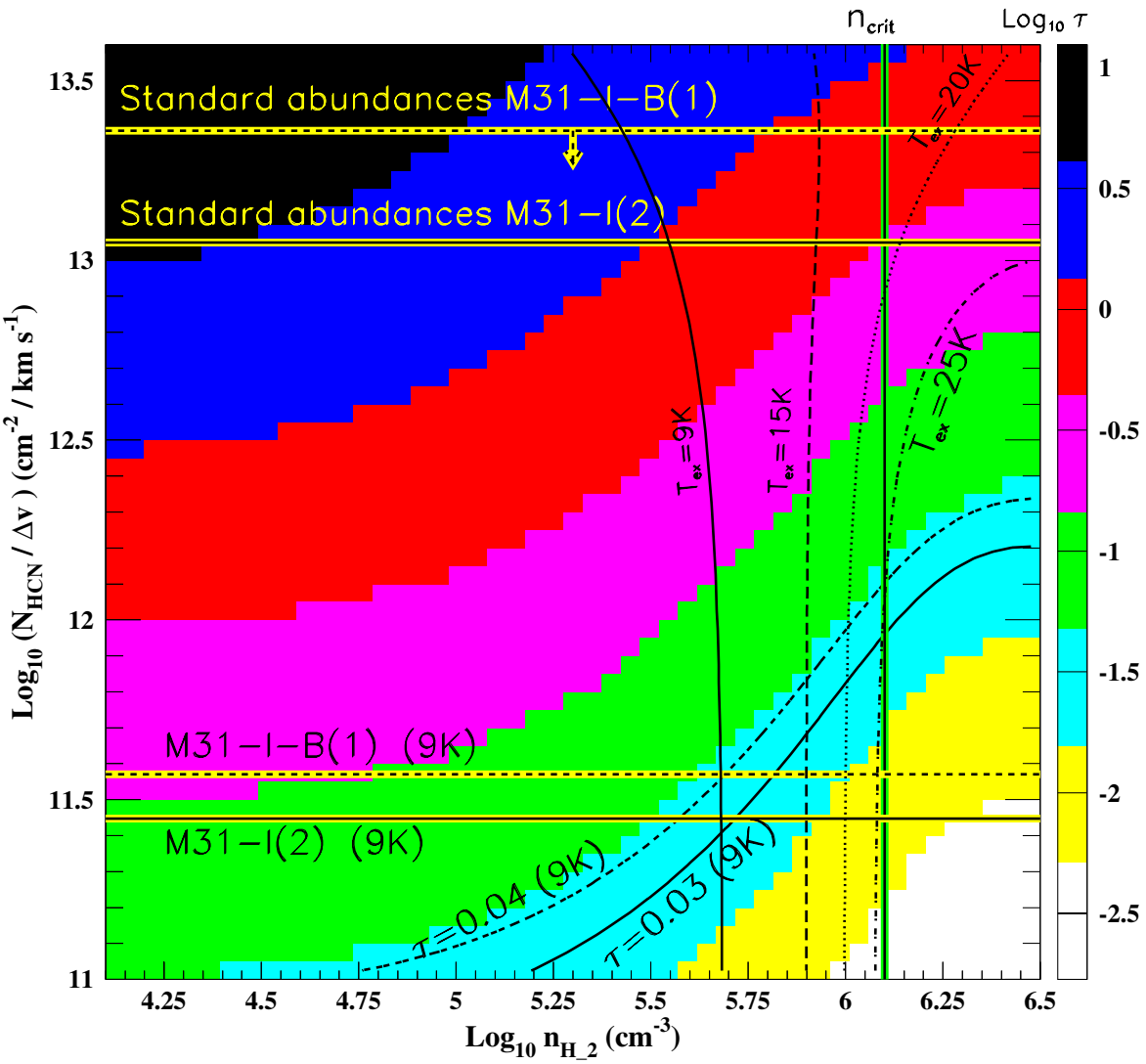

Fig. 11. Main physical parameters corresponding to the HCN gas observed in M31-I(2) and M31-I-B(1). The optical depths are shown as function of the HCN column density (per km s^{-1}) and the molecular hydrogen density n_{H_2}. The corresponding contours for these two clumps are shown with a dashed line for M31-I-B(1) and with a full line for M31-I(2). The vertical (green) line indicates the critical density computed for a collisional temperature of 20 K (see Table 3). The lower horizontal full (dashed) line shows the column density measured for M31-I(2) (M31-I-B(1)) at 9 K. The upper horizontal lines correspond to the column densities computed with standard abundances (Bergin et al. 1995) and the corresponding molecular hydrogen column densities. For M31-I-B(1), we derive an upper limit as the molecular hydrogen column density is only available for a smaller beam (see Table A.1) and we expect some dilution of the signal. The contour levels correspond to excitation temperatures of 9 K (full line), 15 K (dashed line), 20 K (dotted line), and 25 K (dash-dotted line).

5.1. Geometrical configuration of the gas

M31 has been targeted by different surveys. In Sect. 5.1.1, we study the distribution of point sources from different catalogues in search of possible signs of extinction that trace the gas. In Sect. 5.1.2, we summarise the arguments we can derive from the diffuse components.

5.1.1. Point sources and extinction

In Fig. 13, we considered four catalogues: X-ray sources from Stiele et al. (2011), deeper X-ray sources from Hofmann et al. (2013), planetary nebulae from Ciardullo et al. (1989), and UV sources from Rosenfield et al. (2012). The UV sources studied by Rosenfield et al. (2012) trace the old stellar population, and they have the same radial distribution as low-mass X-ray binaries, which correspond to the majority of the X-ray sources in Hofmann et al. (2013). The stellar kinematics has been studied by Saglia et al. (2010) with long slits: bulge stars exhibit a rotation with a maximum velocity of 100 km s^{-1} along the major axis (considered at PA = 48 deg) and a zero (systemic) velocity along the minor axis). These velocities clearly do not correspond to the gas component we detected.

For each catalogue, we plotted the azimuthal distribution of point sources within a radius of 300, 200, and 140″, depending on the area covered. These populations all belong to the same ellipsoid of PA ≃ 52 deg as first discussed by Kaaret (2002). The maxima of the sinusoids correspond to the major axis, while the minima (where our dense gas has been detected) correspond to the minor axis.

The number of sources is significantly larger for Hofmann et al. (2013) than for Stiele et al. (2011); the former work is more sensitive as the data are stacked over a longer period. The work of Rosenfield et al. (2012) based on HST data contains an

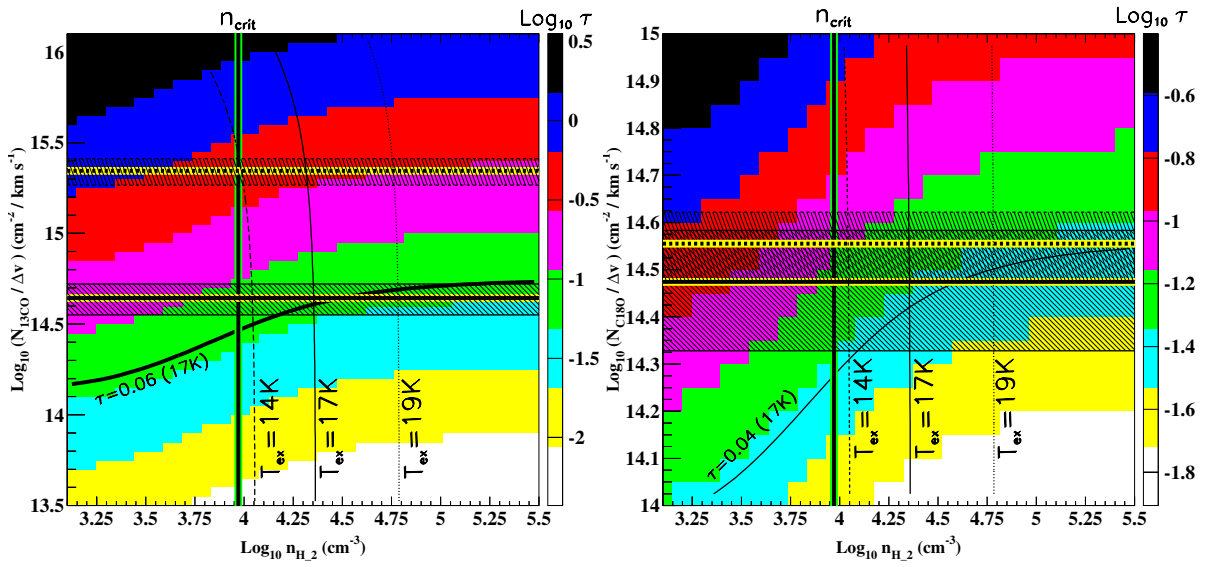

Fig. 12. Main physical parameters corresponding to the ^{13}CO(2–1) gas (*left panel*) and the C^{18}O(2–1) gas (*right panel*) detected in M31-I(3). The optical depths are shown as function of the ^{13}CO(2–1) column density (per km s^{-1}) and the molecular hydrogen density n_{H_2}. The vertical green-black lines indicate the critical densities computed for a collisional temperature of 20 K (see Table 3). The horizontal thick, full yellow-black lines indicate the ^{13}CO(2–1) and the C^{18}O(2–1) averaged column densities (per unit velocity), while the horizontal thin black lines indicate the corresponding 1σ standard deviation; the hatched area corresponds to the M31-I(3) detection. The horizontal thick, dashed yellow-black lines (thin black lines) correspond to the column densities (1σ standard deviation) computed with standard abundances (Bergin et al. 1995) and the corresponding molecular hydrogen column densities. The full line (dashed and dotted) contour levels correspond to an excitation temperature of 17 K (14 K and 19 K). The optical depths, corresponding to 17 K, are shown as a thick line contour level.

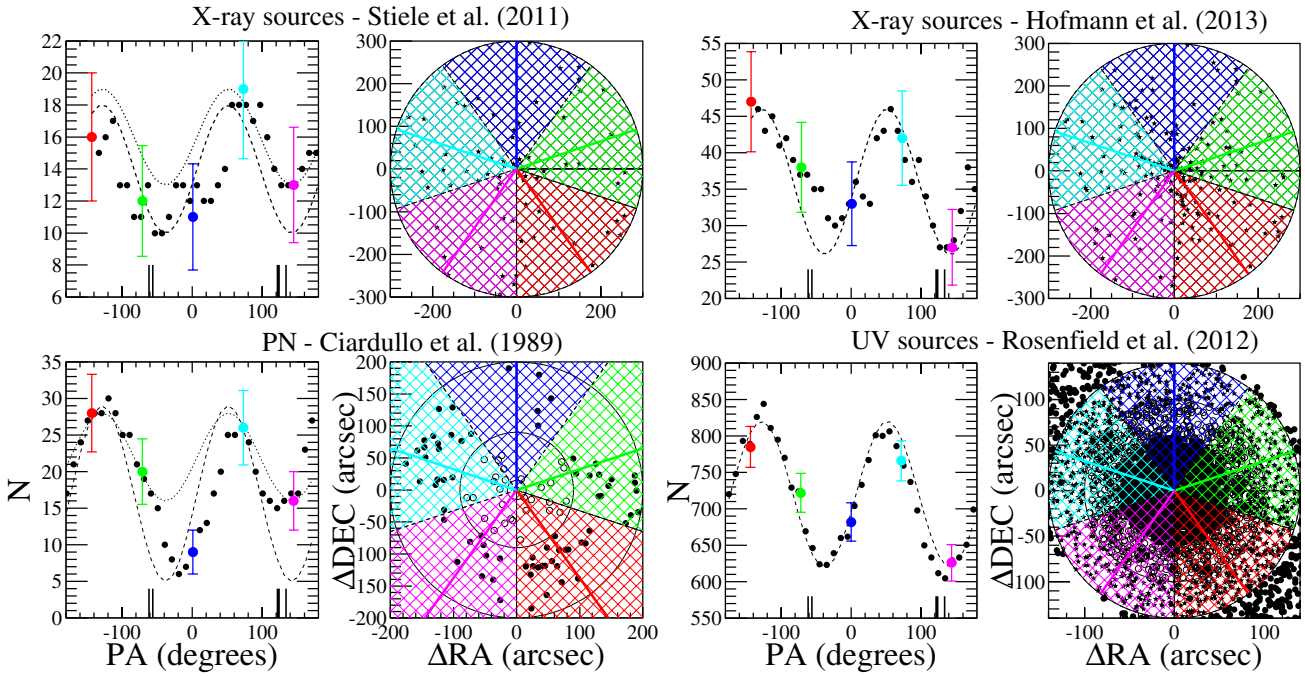

Fig. 13. Azimuthal (1st and 3rd columns) and spatial (2nd and 4th) distribution of X-ray sources (*top*) and planetary nebulae and UV sources (*bottom*). The *top left panels* show the deep *Chandra*-detected X-ray sources from Stiele et al. (2011). The *top right panels* show the X-ray sources from Hofmann et al. (2013). The *bottom left panels* indicate the planetary nebulae from Ciardullo et al. (1989; see also Melchior & Combes 2013). The *bottom right panels* show the HST UV sources from Rosenfield et al. (2012). The dashed line exhibits the best-fit profile from Kaaret (2002) corresponding to a disc with a position angle PA = 52 deg. In the *right panels*, the two minima are roughly at the same level, while in the *left panels* the first is deeper as indicated qualitatively with the dotted line. The ticks in the 1st and 3rd figure columns correspond to the position angles of our detections.

unprecedented number of sources thanks to deep integration and a gain in spatial resolution. We can observe that in these deep observations the two minima of the sinusoid are about at the same level, while the previous observations exhibit an asymmetry. This asymmetry is not really significant when compared to the Poisson error bars shown in the Fig. 13. While in radio we do not expect much extinction, the UV sources in Rosenfield et al. (2012) should be very sensitive to extinction. However, we do

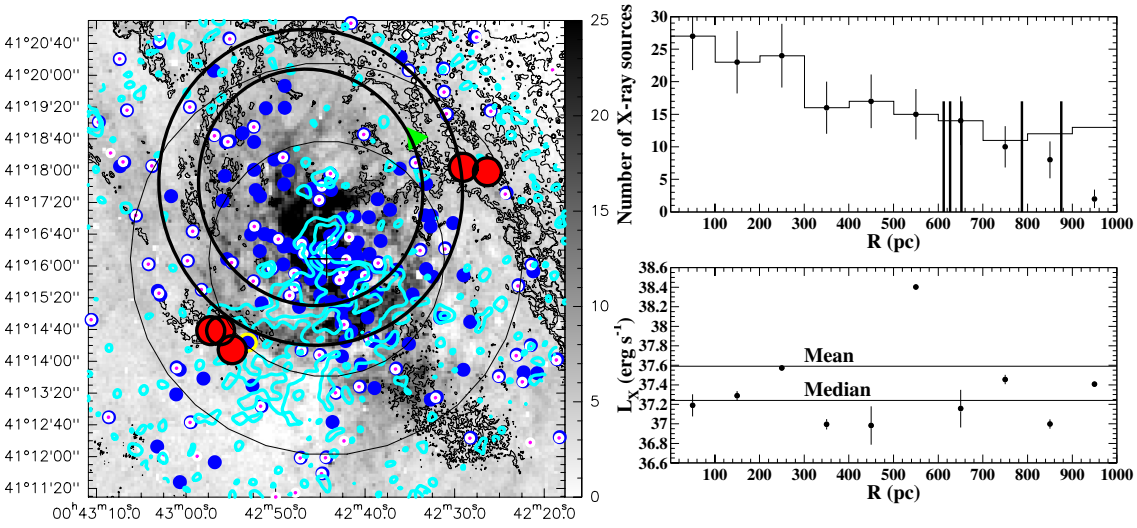

Fig. 14. Known heating sources. On the *left side*, we superimpose on the Hα+[NII] map from Ciardullo et al. (1988): the X-ray sources detected by Hofmann et al. (2013) with blue dots; the 1 Gyr young stellar cluster detected by Kang et al. (2012) with the green triangle; and the X-ray sources detected by Stiele et al. (2011) and Barnard et al. (2014) with white and purple dots. The blue dots with a yellow circle correspond to the first (and more central) ultra-luminous X-ray transient (ULX) detected in M31 (e.g. Kaur et al. 2012). The black contours correspond to the apparent A_B extinction map discussed in Melchior et al. (2000). The light blue contours correspond to the 6 cm polarised intensity detected by Gießübel & Beck (2014). The large red circles correspond to our detections. Light black circles provide typical projected radial distance from the centre (x pc and y pc). Thick ellipses show the approximate position of the inner ring. On the *right side*, we indicate, in the *top panel*, the number of X-ray sources (Hofmann et al. 2013) detected at each radius; in the *bottom panel*, the X-ray luminosity at each radius is shown as a function of the radius. The mean and median values of the X-ray luminosity (averaged in 100 pc radial bin) is also provided.

not detect any strong asymmetry: if we compute the ratio of the numbers of sources from the near and far sides, we find 0.9676 (0.9662) if we consider 52 deg (77 deg). These ratios are significant as they have a Poisson noise of 0.012. If this asymmetry is due to extinction, it affects 4% of the studied area. This order of magnitude is consistent with the gas beam filling factors computed in Sect. 4.3. However, we do not have the sensitivity to derive whether this patchy dust component belongs to the large scale disc (PA = 77 deg) or the more face-on component detected in the stellar bulge population (PA = 52 deg). We can exclude the possibility that young stellar clusters from the disc component could create this inhomogeneity, as no HII region is detected in this area (Azimlu et al. 2011) beside the cluster close to the centre (Lauer et al. 2012). The (young) stellar UV cluster (Kang et al. 2012) closest to our detection has an age of 1 Gyr and is at the offset (−111″,152″) from the centre and at a closest separation of 71 arcsec (271 pc in projection) to our north-western dense gas complex. Dong et al. (2015) detected an intermediate age (300 Myr to 1 Gyr old) stellar population at solar metallicity associated with the bulge, which could contribute up to 50% of the V intensity. However, they only studied the radial dependency, while we expect a smooth spatial distribution as the stars have performed numerous galactic rotations since their birth.

Assuming a uniform distribution in the stellar ellipsoid, one can estimate the ellipticity as done by Kaaret (2002). For the Rosenfield et al. (2012; Hofmann et al. 2013) sample studied here within 140″ (300″), we estimate $\epsilon = 0.24$ ($\epsilon = 0.44$). This is consistent with the measurements of the radial variation of the ellipticity and position angle performed on J-2MASS photometry by Melchior & Combes (see Fig. A.1 2013). This supports our previous finding that there is very little extinction.

While these populations trace the bulge, there is an unexpected X-ray source alignment in the Hofmann et al. (Fig. 14, 2013) catalogue very close to the centre. Similar to that observed in the outskirts of M31 (e.g. McConnachie et al. 2009), these X-ray sources could be part of a tidal stream whose stellar population could be hidden by the crowding at other wavelengths. The facts that it corresponds to an old stellar population and that it is aligned are strong arguments to argue that they are far from the centre and seen in projection. However, it is not aligned with our positions nor any diffuse components discussed below.

5.1.2. Gas components

While the stellar population mainly belongs to the bulge, the diffuse components, apart from the UV to near-IR stellar continuum, are gaseous.

Radio component. The analysis of the radio emission (Gießübel & Beck 2014) reveals complementary information. There is a significant continuum flux at 3.6 cm and 6.2 cm, and a weak polarised component (∼10%). There is a relatively flat spectral index ($\nu^{\beta=-0.4}$), while the contribution from the black hole is very weak and localised (Li et al. 2011). This flat spectral index cannot be accounted for by an inverted synchrotron emission due to a present AGN, but we cannot exclude relic emission from past AGN activity (e.g. Ishibashi & Fabian 2015). The flat spectral index could be due to the combination of synchrotron and free-free emissions. In the Block et al. (2006) scenario, the inner ring forms and expands to its actual position in ∼150 Myr. The corresponding past starburst activities (150–200 Myr old) could account for the continuum emission stronger close to the centre. The polarisation map of Gießübel & Beck (2014) is illustrated as contours in Fig. 14. The polarisation is blurred by the Faraday rotation of the electrons. On the north side, no polarisation is detected, while it is detected on the south side. This polarisation pattern corresponds to a good approximation to the simple modelling proposed in Melchior & Combes (see Fig. 16 and Table 7, 2011) of the inner ring with a PA of −35 deg and an inclination of 40 deg, together with the two discs components strongly depolarising the north-western side. In addition in

the south side, we clearly see some inhomogeneities in the polarised emission detected: there is a gap that corresponds to the H_α(+[NII]) emission. This confirms the parameters of the inner ring's location on the near side, i.e. in the south-east direction. This supports some previous tentative interpretations (Ciardullo et al. 1988) that we are observing structures more face-on than the 77 deg main disc with the near side on the north side and a more edge-on structure on the south side.

Supporting the post-starburst scenario, the central field exhibits a remmant tidal swirl observed in radio at 3.6 cm and 6.2 cm (Gießübel & Beck 2014) and in ionised gas (Ciardullo et al. 1988). These radio emissions could trace relic activities of stellar populations younger than 200 Myr (Condon 1992) i.e. following the impact and expansion of the inner ring. This remnant tidal swirl could be dominated by shocks, e.g. from supernovae as [NII] is larger than H_α (Rubin et al. 1972), while the inner ring is possibly stronger in H_α tracing a 200 Myr old starburst (Block et al. 2006).

Ionised gas. While we know that the observed extinction is weak and the overall amount of gas is small, Melchior et al. (2000) has estimated a lower limit on A_B assuming all the gas is in front of the bulge. Even in locations where the extinction detected is small (i.e. probably underestimated by the previous assumption), it corresponds well with features detected in the infrared (e.g. at 100 μm as indicated in Fig. 1). As discussed by Ford et al. (2013), the central gas is hotter than the inner ring. The 100 μm map exhibits hot dust and cold dust, while the 500 μm map mainly shows cold dust in the inner ring (close to our observed positions). This central hot component corresponds to the ionised gas (Ciardullo et al. 1988). The ionsed gas is very inhomegeneous and its distribution does not exhibit any clear sign of extinction. This is compatible with the fact that the gas is very clumpy with a filling factor smaller than 1%and that the near/far-side asymmetry, possibly due to extinction, is at the level of 4%.

Molecular gas. Our dense gas detections discussed here exhibit a surprising velocity pattern. This is the wavelength range where the best velocity resolution is achieved (few km s^{-1}), and we observe in two positions along the minor axis where the systemic velocity is expected atvelocities between −530 and −140 km s^{-1}. This kinematical information demonstrates the presence of several molecular gas components along these lines of sight. In contrast to HI measurements (Braun et al. 2009; Chemin et al. 2009), we do not have a priori the sensitivity to detect molecular gas in the warp or the external parts of the galaxy.

5.2. Heating sources

We investigate here the possible heating sources, which could explain why the signal is stronger on one side and what heats the gas in general. Following Bogdán & Gilfanov (2008), we know that the diffuse X-ray gas detected in this area within 150–200″ from the centre is weak. The detected 0.5–1.2 keV flux lies in the range 1.6–9 × 10^{-18} erg s^{-1} cm^{-2} arcsec^{-2}, considering a molecular cloud of 1 pc with a distance of M31 of 780 kpc, we can estimate a rough X-ray incident radiation intensity of 6–34 × 10^{-7} erg s^{-1} cm^{-2}. This is at least five orders of magnitude weaker than the radiation field considered by Meijerink et al. (2007) for XDR modelling. There is only one ROSAT (Second ROSAT PSPC catalogue) source within 12″ (22″) from M31I (M31I-B) with a 14 arcsec positional error, with a flux of 10^{-12} erg s^{-1} cm^{-2} arcsec^{-2}.

There is an ultra-luminous X-ray source (Kaur et al. 2012) located 22″ from M31-2c-a, which has exhibited an outburst that lasted three months. ULX are correlated with star formation (Mapelli et al. 2009). As in the Cartwheel, this ULX is detected next to the inner ring. The presence of ULX in the ring supports the starburst scenario, as several ULX are detected in ring galaxies suspected of frontal collision (Prestwich et al. 2012). ULX are expected in low-metallicity environments (Prestwich et al. 2013), which could explain why only one has been detected. Barnard et al. (2012) measured an outburst flux of 50 × 10^{37} erg s^{-1}, which could contribute at the level of 5 × 10^{-3} erg s^{-1} cm^{-2}.

In this inner region, the contribution of the central black hole could be significant. However, Li et al. (2011) measured a burst of activity in January 2006 with *Chandra* X-Ray Observatory at a level of 4.3 × 10^{37} erg s^{-1} and a quiescent level of 4.8 × 10^{36} erg s^{-1}. At the distance of M31I and M31I-B (supposed in the sky plane), this would contribute to the X-ray incident radiation intensity at a level of 6.9 and 5.5 × 10^{-8} erg s^{-1} cm−2 (6.2 and 5.0 × 10^{-7} erg s^{-1} cm^{-2}) in the quiescent state (during the outburst). This is four to five orders of magnitude weaker than the possible contribution of the ULX discussed above.

The X-ray sources shown in Fig. 14 are strongly concentrated towards the centre. The catalogue Hofmann et al. (2013) based on *Chandra* HRC is more sensitive than other catalogues (Stiele et al. 2011; Barnard et al. 2014). The surface density varies as $(R/1\,\mathrm{kpc})^{-2.5}$. The contribution of the central part is thus more important than the black hole activity.

We can thus exclude that the excitation mechanism of the gas is due to X-ray radiation from the gas accreted by the black hole. The [OIII] line emissions detected by Saglia et al. (2010) and M. Sarzi (priv. comm.) can be accounted for by planetary nebulae and no LINER activity is necessary.

The heating is mainly due to the old stellar population as discussed by Draine et al. (2014) and Viaene et al. (2014). Transient X-ray sources, such as ULX, could contribute inhomogeneously to the heating. The heating rate U, based on Mathis et al. (1983) and computed by Draine et al. (2014), are provided in Table 1. The area around M31I and M31I-B have $U = 1.5$, while the other three positions have U in the range 1.8–2.7. This corresponds to an average dust temperature of 20 K, according to Draine et al. (2014).

5.3. Different velocity components

The kinematics of this area is complex with up to three different velocity components. The probability that the warp component, coming from radii larger than 15–20 kpc, is seen in CO emission towards the centre is negligible. This is the case because of the weak metallicity of this gas, which makes it undetectable in CO. As discussed in Melchior & Combes (2011), if we consider that the probability of chance alignment of gas is low and that the gas is inside the main galaxy, this means that we are in the presence of several structures. Indeed, an explanation in terms of non-circular motions in a possible barred potential has already been ruled out given the velocity disposition and the fact that the gas distribution is not aligned with any elongated structure, but in an off-centred ring (Melchior & Combes 2011). The component at the systemic velocity is compatible with gas along the minor axis of the main disc, while the two counter-rotating components could be orbiting in two planes with different inclinations and orientations. They could correspond to an inclined disc and to the inner 1-kpc ring. However, in presence of observations in two positions, it is difficult to fully constrain such a

configuration. Apart from the inner ring detected in infrared (see Fig. 1 and Block et al. 2006) and the H_α(+[NII]) structure detected inside (Ciardullo et al. 1988), we do not have kinematic observations covering these positions. Boulesteix et al. (1987) got the [NII] velocity field within a $3' \times 3'$ field and Nieten et al. (2006) did not integrate deep enough in the central part to detect CO. Opitsch et al. (2015) has detected two rotating components in [OIII], but their two components rotate in the same direction, which adds complexity to the problem. Interestingly, the polarisation map of Gießübel & Beck (2014) corresponds to the parameters proposed by Melchior & Combes (2011) for the three-component modelling.

Finally, the amplitudes between our different velocity components are different and larger than the simulated modulation proposed by Dierickx et al. (2014).

The alternative interpretation is that we are observing gas superimposed on the central part of M31, i.e. gas in the outskirts of the disc (Koch et al. 2015; Lehner et al. 2015; Wolfe et al. 2013; Lockman et al. 2012) is ruled out. No high velocity clouds have been detected in CO (Combes & Charmandaris 2000; Miville-Deschênes et al. 2005), while Galactic gas should be around 0 km s^{-1}.

5.4. ^{13}C depletion and evidence for a post-starburst scenario

In Sect. 4.1, we discussed that it is remarkable that the C^{18}O detection is at a level comparable to the ^{13}CO detection, in contrast to what is observed in the Galaxy (e.g. Nishimura et al. 2015; Shimajiri et al. 2014), where the C^{18}O is usually 10 to 150 times weaker than ^{13} CO. In Table 6, we have shown that ^{13}CO and C^{18}O are optically thin, so we can claim that the ^{13}CO is under-abundant with respect to C^{18}O. In Sect. 4.5, we have shown that these two CO components are close to thermal equilibrium. Hence, we can rely on the abundance ratios computed in Table 7; the deficit is five to ten times weaker than with the Galactic abundances. This deficit could be accounted for by a post-starburst scenario. This kind of ^{13}CO deficit was first observed by Casoli et al. (1991) in post-merger. Davis (2014) also find an anti-correlation of ^{13}CO and star formation and gas surface densities in local galaxies.

This could be the signature of a 200 Myr old starburst triggered by a collision with a galaxy like M32, as proposed by Block et al. (2006). This scenario accounts for the two off-centred ring structures of M31, with most star formation in the 10 kpc ring (Ford et al. 2013) and a smaller ring, where we have detected CO and dense gas.

6. Conclusion

We have detected ^{12}CO(2–1) and ^{13}CO(2–1) lines with multiple velocity components along the minor axis of M31 on both sides of the inner 1-kpc ring. We detected dense gas traced by C^{18}O(2–1), HCN(1–0), and HCO+(1–0) on the north-west side at the systemic velocity for C^{18}O(2–1) and in the blue-shifted component for HCN(1–0) and HCO+(1–0). We also detected a redshifted component for the three molecules by stacking at the CO velocity on both sides.

Draine et al. (2014) and Viaene et al. (2014) found lower measurements for the stellar heating in this area on the north-west side, which could explain why dense gas has only been detected directly on this side. A careful analysis has shown that ^{12}CO is optically thick while the other CO lines are optically thin and close to LTE at an excitation temperature of 17.5–20 K. The gas is very clumpy and the averaged beam filling factor is 0.8%. The average column density of molecular hydrogen is 16×10^{22} cm^{-2}. The derived abundances are all smaller than the standard abundances, but for C^{18}O. The comparison of the derived abundances with RADEX simulations shows that the HCN and HCO+ gas correspond to dense clumps with molecular hydrogen density of the range $1\text{–}6 \times 10^5$ cm^{-3} and an excitation temperature of 9 K. The HCO+/HCN line ratio is comparable with that measured for clouds detected in M31's disc (Brouillet et al. 2005), while the derived abundances are smaller than the Galactic abundances (Bergin et al. 1995), with a larger discrepancy for HCN(1–0). Only one transient ULX object has been identified as a possible secondary source of heating, while the bulge stellar population is sufficient to heat the gas and reproduce the infrared maps.

Our isotopic CO lines and HCN/HCO+ lines detections are all weak and close to the detection limits. We detected C^{18}O in a single point at the systemic velocity. Stacking of all ^{13}CO detections has revealed the underlying presence of C^{18}O gas in the redshifted component. Both the single point and the stacking detections have an overall intensity comparable to ^{13}CO. As we expect C^{18}O to be six times less abundant than ^{13}CO and the measured abundance of C^{18}O is compatible with the standard abundance, ^{13}CO should be depleted. A coherent explanation is that ^{12}C has been enriched during the recent staburst and ^{13}CO had no time to catch up, so it appears depleted. This is compatible with the Block et al. (2006) scenario suggesting a frontal collision with a nearby companion galaxy such as M 32. This collision explains the rings and has triggered a starburst at the epoch of the collision. This is also in agreement with the central starburst, which occured next to the black hole 200 Myr ago (Lauer et al. 2012).

We confirm the presence of three kinematical components detected in molecular gas, as first discussed in Melchior & Combes (2011). Separated by 400 km s^{-1} and on both sides of the systemic velocity, this configuration on the minor axis is not expected for a disc in rotation and cannot be accounted for by a bar. We have also checked that the parameters we first proposed for a simple modelling of the three kinematical components are compatible with other observations. In addition to the 77 deg main disc with a position angle (PA = 35 deg) detected in HI, there is an less inclined nuclear disc (i = 43 deg) with PA = 53 deg (rather than 70 deg, as initially thought). The position angle of this nuclear disc is well defined with different stellar sources catalogues (Kaaret 2002; Rosenfield et al. 2012). The 1-kpc ring with i = 40 deg and PA = −35 deg accounts for the polarised map of Gießübel & Beck (2014) very well.

Acknowledgements. We thank the IRAM staff in Granada for their help during the observations. We are most grateful to S. Viaene for providing us with the maps produced in the Viaene et al. (2014) paper. We used GALEX and ROSAT archive data in Sect. 5.2. We thank the anonymous referee for his useful comments, which improved the paper.

References

André, P., Di Francesco, J., Ward-Thompson, D., et al. 2014, Protostars and Planets VI, 27
Azimlu, M., Marciniak, R., & Barmby, P. 2011, AJ, 142, 139
Bacon, R., Emsellem, E., Combes, F., et al. 2001, A&A, 371, 409
Barnard, R., Galache, J. L., Garcia, M. R., et al. 2012, ApJ, 756, 32
Barnard, R., Garcia, M. R., Primini, F., et al. 2014, ApJ, 780, 83
Bender, R., Kormendy, J., Bower, G., et al. 2005, ApJ, 631, 280
Bergin, E. A., Langer, W. D., & Goldsmith, P. F. 1995, ApJ, 441, 222
Berkhuijsen, E. M., & Fletcher, A. 2015, MNRAS, 448, 2469
Block, D. L., Bournaud., F., Combes, F., et al. 2006, Nature, 443, 832

Bogdán, Á., & Gilfanov, M. 2008, MNRAS, 388, 56
Bohlin, R. C., Savage, B. D., & Drake, J. F. 1978, ApJ, 224, 132
Boulesteix, J., Georgelin, Y. P., Lecoarer, E., Marcelin, M., & Monnet, G. 1987, A&A, 178, 91
Braun, R., Thilker, D. A., Walterbos, R. A. M., & Corbelli, E. 2009, ApJ, 695, 937
Brouillet, N., Muller, S., Herpin, F., Braine, J., & Jacq, T. 2005, A&A, 429, 153
Buchbender, C., Kramer, C., Gonzalez-Garcia, M., et al. 2013, A&A, 549, A17
Carlstrom, J. E. 1988, Molecular Clouds, Milky-Way and External Galaxies, 315, 405
Casoli, F., Dupraz, C., Combes, F., & Kazes, I. 1991, A&A, 251, 1
Chemin, L., Carignan, C., & Foster, T. 2009, ApJ, 705, 1395
Ciardullo, R., Rubin, V. C., Ford, W. K., Jr., Jacoby, G. H., & Ford, H. C. 1988, AJ, 95, 438
Ciardullo, R., Jacoby, G. H., Ford, H. C., & Neill, J. D. 1989, ApJ, 339, 53
Combes, F., & Charmandaris, V. 2000, A&A, 357, 75
Condon, J. J. 1992, ARA&A, 30, 575
Crane, P. C., Dickel, J. R., & Cowan, J. J. 1992, ApJ, 390, L9
Crocker, A., Krips, M., Bureau, M., et al. 2012, MNRAS, 421, 1298
Dame, T. M., Hartmann, D., & Thaddeus, P. 2001, ApJ, 547, 792
Davis, T. A. 2014, MNRAS, 445, 2378
Dierickx, M., Blecha, L., & Loeb, A. 2014, ApJ, 788, L38
Dong, H., Li, Z., Wang, Q. D., et al. 2015, MNRAS, 451, 4126
Draine, B. T., & Li, A. 2007, ApJ, 657, 810
Draine, B. T., Aniano, G., Krause, O., et al. 2014, ApJ, 780, 172
Ford, G. P., Gear, W. K., Smith, M. W. L., et al. 2013, ApJ, 769, 55
Garcia, M. R., Hextall, R., Baganoff, F. K., et al. 2010, ApJ, 710, 755
Gießübel, R., & Beck, R. 2014, A&A, 571, A61
Ginsburg, A., Darling, J., Battersby, C., Zeiger, B., & Bally, J. 2011, ApJ, 736, 149
Greve, A., Baars, J. W. M., Peñalver, J., & LeFloch, B. 1996, Radio Science, 31, 1053
Groves, B., Krause, O., Sandstrom, K., et al. 2012, MNRAS, 426, 892
Hofmann, F., Pietsch, W., Henze, M., et al. 2013, A&A, 555, A65
Hirota, T., Yamamoto, S., Mikami, H., & Ohishi, M. 1998, ApJ, 503, 717
Ishibashi, W., & Fabian, A. C. 2015, MNRAS, 451, 93
Kang, Y., Rey, S.-C., Bianchi, L., et al. 2012, ApJS, 199, 37
Kaaret, P. 2002, ApJ, 578, 114
Kaur, A., Henze, M., Haberl, F., et al. 2012, A&A, 538, A49
Koch, A., Danforth, C. W., Rich, R. M., Ibata, R., & Keeney, B. A. 2015, ApJ, 807, 153
Krips, M., Crocker, A. F., Bureau, M., Combes, F., & Young, L. M. 2010, MNRAS, 407, 2261
Lauer, T. R., Bender, R., Kormendy, J., Rosenfield, P., & Green, R. F. 2012, ApJ, 745, 121
Lehner, N., Howk, J. C., & Wakker, B. P. 2015, ApJ, 804, 79
Li, Z., Garcia, M. R., Forman, W. R., et al. 2011, ApJ, 728, L10
Li, F.-C., Wu, Y.-W., & Xu, Y. 2015, Res. Astron. Astrophys., 15, 785
Liu, X.-L., Wang, J.-J., & Xu, J.-L. 2013, MNRAS, 431, 27
Liu, X.-L., Wang, J.-J., & Xu, J.-L. 2014, MNRAS, 443, 2264
Lockman, F. J., Free, N. L., & Shields, J. C. 2012, AJ, 144, 52
McConnachie, A. W., Irwin, M. J., Ibata, R. A., et al. 2009, Nature, 461, 66
Mangum, J. G., & Shirley, Y. L. 2015, PASP, 127, 266
Mapelli, M., Colpi, M., & Zampieri, L. 2009, MNRAS, 395, L71
Mathis, J. S., Mezger, P. G., & Panagia, N. 1983, A&A, 128, 212
Matsushita, S., Kawabe, R., Kohno, K., Tosaki, T., & Vila-Vilaró, B. 2010, PASJ, 62, 409
Mauersberger, R., Henkel, C., Weiß, A., Peck, A. B., & Hagiwara, Y. 2003, A&A, 403, 561
Meijerink, R., Spaans, M., & Israel, F. P. 2007, A&A, 461, 793
Melchior, A.-L., & Combes, F. 2011, A&A, 536, A52
Melchior, A.-L., & Combes, F. 2013, A&A, 549, A27
Melchior, A.-L., Viallefond, F., Guélin, M., & Neininger, N. 2000, MNRAS, 312, L29
Miville-Deschênes, M.-A., Boulanger, F., Reach, W. T., & Noriega-Crespo, A. 2005, ApJ, 631, L57
Nieten, C., Neininger, N., Guélin, M., et al. 2006, A&A, 453, 459
Nishimura, A., Tokuda, K., Kimura, K., et al. 2015, ApJS, 216, 18
Opitsch, M., Fabricius, M., Saglia, R., Bender, R., & Williams, M. 2015, IAU Symp., 309, 334
Prestwich, A. H., Galache, J. L., Linden, T., et al. 2012, ApJ, 747, 150
Prestwich, A. H., Tsantaki, M., Zezas, A., et al. 2013, ApJ, 769, 92
Rosenfield, P., Johnson, L. C., Girardi, L., et al. 2012, ApJ, 755, 131
Rubin, V. C., Krishna Kumar, C., & Ford, W. K., Jr. 1972, ApJ, 177, 31
Saglia, R. P., Fabricius, M., Bender, R., et al. 2010, A&A, 509, A61
Savage, C., & Ziurys, L. M. 2004, ApJ, 616, 966
Schilke, P., Walmsley, C. M., Pineau Des Forets, G., et al. 1992, A&A, 256, 595
Schinnerer, E., Weiß, A., Aalto, S., & Scoville, N. Z. 2010, ApJ, 719, 1588
Schöier, F. L., van der Tak, F. F. S., van Dishoeck, E. F., & Black, J. H. 2005, A&A, 432, 369
Shimajiri, Y., Kitamura, Y., Saito, M., et al. 2014, A&A, 564, A68
Shirley, Y. L. 2015, PASP, 127, 299
Smith, M. W. L., Eales, S. A., Gomez, H. L., et al. 2012, ApJ, 756, 40
Stiele, H., Pietsch, W., Haberl, F., et al. 2011, A&A, 534, A55
Strong, A. W., Bloemen, J. B. G. M., Dame, T. M., et al. 1988, A&A, 207, 1
Tan, Q.-H., Gao, Y., Zhang, Z.-Y., & Xia, X.-Y. 2011, Res. Astron. Astrophys., 11, 787
van der Tak, F. F. S., Black, J. H., Schöier, F. L., Jansen, D. J., & van Dishoeck, E. F. 2007, A&A, 468, 627
Viaene, S., Fritz, J., Baes, M., et al. 2014, A&A, 567, A71
Wilson, T. L., & Rood, R. 1994, ARA&A, 32, 191
Wolfe, S. A., Pisano, D. J., Lockman, F. J., McGaugh, S. S., & Shaya, E. J. 2013, Nature, 497, 224
Wu, Y., Liu, T., Meng, F., et al. 2012, ApJ, 756, 76

Appendix A: Additional table and figures

Table A.1. Results.

Pos.	V_0 (km s^{-1})			Δv (km s^{-1})			$T_{\rm Peak}$ (mK)			$I_{\rm Line}$ (K km s^{-1})			$I_{^{12}CO}/I_{^{13}CO}$	$I_{^{12}CO}/I_{C^{18}O}$
(2–1)	^{12}CO	^{13}CO	C^{18}O	^{12}CO	^{13}CO	C^{18}O	^{12}CO	^{13}CO	C^{18}O	^{12}CO	^{13}CO	C^{18}O		
I(1)	–144.2 ± 0.2	–144.2∗		7.5 ± 0.5	6.3 ± 1.5		422	20.0		3.4 ± 0.2	0.16 ± 0.02	<0.056	22.1 ± 2.9	>61
I(2)	–402. ± 3	–402∗		62 ± 12	62∗		146	4.8		9.6 ± 0.5	0.31 ± 0.06	<0.22	31.0 ± 6.2	>44.
I(3)	–291. ± 9	–291∗	–291∗	69 ± 18	69∗	69∗	77	4.2	2.9	6 ± 1	0.31 ± 0.06	0.21 ± 0.06	19.3 ± 4.9	28.6 ± 9.5
I-B(1)	–463.0 ± 0.7	–463∗		38 ± 2	38∗		356	11.5		14.3 ± 0.6	0.47 ± 0.04	<0.10	30.4 ± 2.9	>143.
I-B(2)	–397. ± 7	–397∗		66. ± 14	66∗		49.2	4.2		3.5 ± 0.7	0.28 ± 0.05	<0.51	12.5 ± 3.4	>6.9
2d-a(1)	–523.0 ± 0.9	–522 ± 3		21. ± 3	25 ± 7		99.8	5.7		2.2 ± 0.2	0.15 ± 0.03	<0.13	15. ± 3	>16.9
2d-a(2)	–234. ± 1	–225 ± 4		37. ± 3	40 ± 11		105	5.2		4.1 ± 0.3	0.19 ± 0.04	<0.17	22. ± 5	>24.1
2d-b(1)	–211.5 ± 0.7	–211∗		30 ± 2	30∗		176	3.2		5.5 ± 0.3	0.10 ± 0.03	<0.06	55.0 ± 17	>91.7
2d-b(2)	–269. ± 3	–269∗		46 ± 6	46∗		44	2.7		2.1 ± 0.3	0.13 ± 0.04	<0.09	16. ± 5	>23.3
2d-b(3)	–526. ± 2	–526∗		20 ± 8	20∗		38	4.8		0.8 ± 0.2	0.10 ± 0.03	<0.09	8. ± 3	>8.9
2c-a(1)	–243 ± 3	–241 ± 13		57 ± 4	97 ± 28		61	4.2		3.7 ± 0.3	0.44 ± 0.11	<0.30	8.4 ± 2.2	>12.3
2c-a(2)	–223.9 ± 0.6			10 ± 2			54			0.58 ± 0.15	<0.09	<0.11	>5.8	>4.8
2c-a(3)	–204.7 ± 0.4			12.6 ± 0.9			98			1.31 ± 0.15	<0.09	<0.12	>14.6	>9.4
(1–0)	^{12}CO			^{12}CO			^{12}CO			^{12}CO			N_{H_2} (10^{22} cm^{-2})	
I(1)	–144.2 ± 0.2			9.3 ± 0.4			322			3.2 ± 0.1			2.24 ± 0.07	
I(2)	–404.2 ± 0.9			49 ± 3			140			7.3 ± 0.3			14.8 ± 0.6	
I(3)	–278 ± 3			77 ± 14			54			2.7 ± 0.2			10.4 ± 0.8	

Pos.	$I_{\rm Line}$ (K km s^{-1})						Molecular column densities (hypothesis: LTE, optically thin, $\eta_{\rm bf}$, 20K) (cm^{-2})				N_{H_2} (cm^{-2})
	SiO (2–1)	CCH (1–0)	SiO (5–4)	H_2CO (3_{03}–2_{02})	H_2CO (3_{22}–2_{21})	H_2CO (3_{21}–2_{20})	$N_{^{13}CO}$ (10^{16})	$N_{C^{18}O}$ (10^{16})	N_{HCN} (10^{13})	N_{HCO+} (10^{13})	(10^{22})
I (1)	<0.06	<0.09	<0.12	<0.13	<0.16	<0.09	0.29 ± 0.04	<0.10	<0.77	<0.44	3.0 ± 0.2
I (2)	<0.06	<0.09	<0.12	<0.13	<0.16	<0.09	1.64 ± 0.32	<1.16	2.73 ± 0.75	2.41 ± 0.43	24.3 ± 1.3
I (3)	<0.06	<0.09	<0.12	<0.13	<0.16	<0.09	3.11 ± 0.60	2.10 ± 0.60	<4.24	<2.42	28.8 ± 4.8
I-B (1)	<0.08	<0.09	<0.10	<0.09	<0.10	<0.09	1.02 ± 0.09	<0.22	2.04 ± 0.41	1.98 ± 0.23	14.9 ± 0.2
I-B (2)	<0.08	<0.09	<0.10	<0.09	<0.10	<0.09	4.40 ± 0.78	<7.99	<8.85	<5.06	26.3 ± 2.3
2d-a(1)	<0.08	<0.09	<0.08	<0.08	<0.10	<0.08	1.16 ± 0.23	<1.00	<4.72	<2.29	8.2 ± 0.6
2d-a(2)	<0.08	<0.09	<0.08	<0.08	<0.10	<0.08	1.40 ± 0.29	<1.25	<4.49	<2.17	14.4 ± 1.1
2d-b(1)	<0.08	<0.061	<0.11	<0.09	<0.09	<0.09	0.44 ± 0.14	<0.26	<2.68	<1.53	11.6 ± 0.6
2d-b(2)	<0.08	<0.061	<0.11	<0.09	<0.09	<0.09	2.28 ± 0.70	<1.58	<10.72	<6.13	17.7 ± 2.5
2d-b(3)	<0.08	<0.061	<0.11	<0.09	<0.09	<0.09	2.03 ± 0.60	<1.83	<12.41	<7.09	7.8 ± 1.9
2c-a(1)	<0.08	<0.24	<0.19	<0.05	<0.14	<0.08	5.57 ± 1.39	<3.79	<11.89	<6.80	22.4 ± 1.8
2c-a(2)	<0.08	<0.24	<0.19	<0.05	<0.14	<0.08	<1.28	<1.57	<13.44	<7.68	4.0 ± 1.0
2c-a(3)	<0.08	<0.24	<0.19	<0.05	<0.14	<0.08	<0.71	<0.94	<7.40	<4.23	4.9 ± 0.6

Pos.	V_0 (km s^{-1})		Δv (km s^{-1})		$T_{\rm Peak}$ (mK)		$I_{\rm line}$ (K km s^{-1})					
	HCO+ (1–0)	HCN (1–0)	HCO+ (1–0)	HCN (1–0)	HCO+ (1–0)	HCN (1–0)	HCO+ (1–0)	HCN (1–0)	HNC (1–0)	HC3N (10-9)	HOC+ (1–0)	HNCO (4-3)
I(2)	–402 ± 4	–425 ± 10	54 ± 8	57 ± 18	3.0	1.7	0.17 ± 0.03	0.11 ± 0.03	<0.12	<0.12	<0.10	<0.10
I-B(1)	–473 ± 4	–471 ± 3	54 ± 8	32 ± 8	5.8	5.8	0.34 ± 0.04	0.20 ± 0.04	<0.07	<0.07	<0.07	<0.08
2d-a							<0.11	<0.13	<0.10	<0.12	<0.13	<0.13
2d-b							<0.13	<0.13	<0.09	<0.10	<0.11	<0.07
2c-a							<0.20	<0.18	<0.21	<0.22	<0.20	<0.18

Notes. Right: CO(2–1) line fit results: $I_{\rm CO}$ upper limits are provided at 3σ for the ^{13}CO (or ^{12}CO) velocity dispersion; middle: 3σ upper limits on molecular lines observed in the LO (Lower Outer) band (with σ = 32 km s^{-1}); column densities are corrected for beam-filling factors; hydrogen column density are derived from ^{12}CO measurements as discussed in Sect. 3 with a Galactic $X_{\rm CO}$ factor. *Left:* HCO+(1–0) and HCN(1–0) Line fit results; HNC(1–0), HNCO(4–3), HOC+(1–0) and HC3N(10–9) upper limits provided at $3\Delta v$ (assuming σ = 54 km s^{-1}).

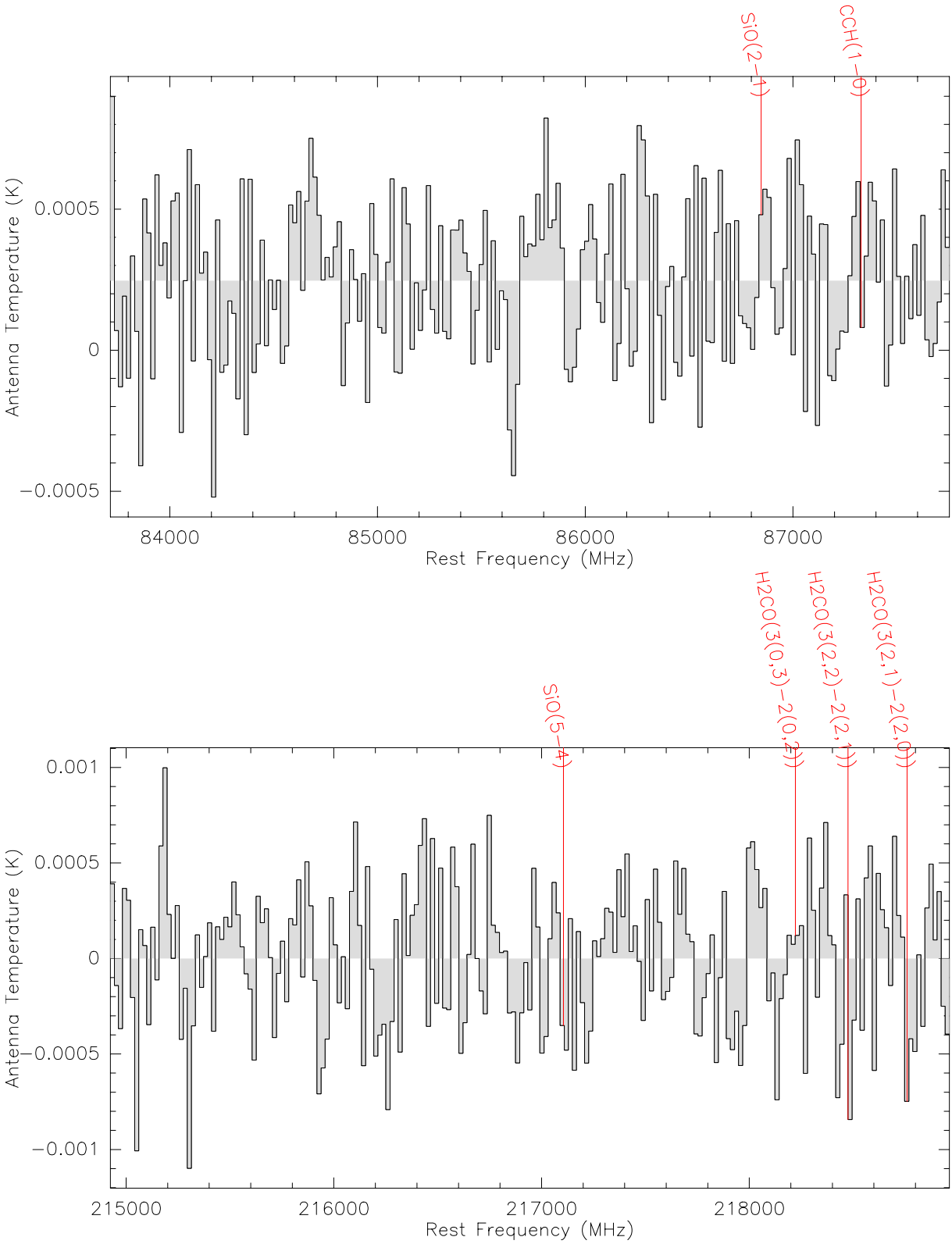

Fig. A.1. Averaging of the observations performed in the EMIR lower outer (LO) bands. The different lines present in the bandwidth are plotted in the rest-frame frequency. No signal is detected. This has been used to derived detection limit in Table A.1.

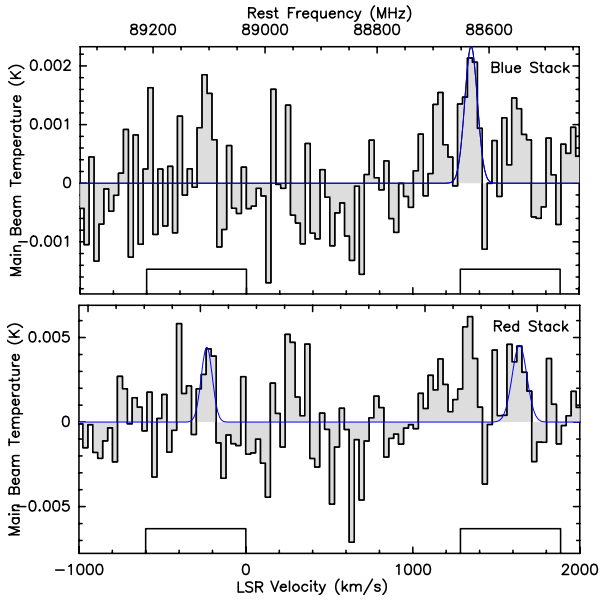

Fig. A.2. HCN(1–0) and HCO+(1–0) stacking of the south-east positions. The stacking is based on the ^{13}CO velocities. The *top* (*bottom*) *panel* shows the stacking corresponding to >–300 km s^{-1} (<–300 km s^{-1}) velocities. The velocities are shown in the rest-frame frequency of the HCO+(1–0) line.

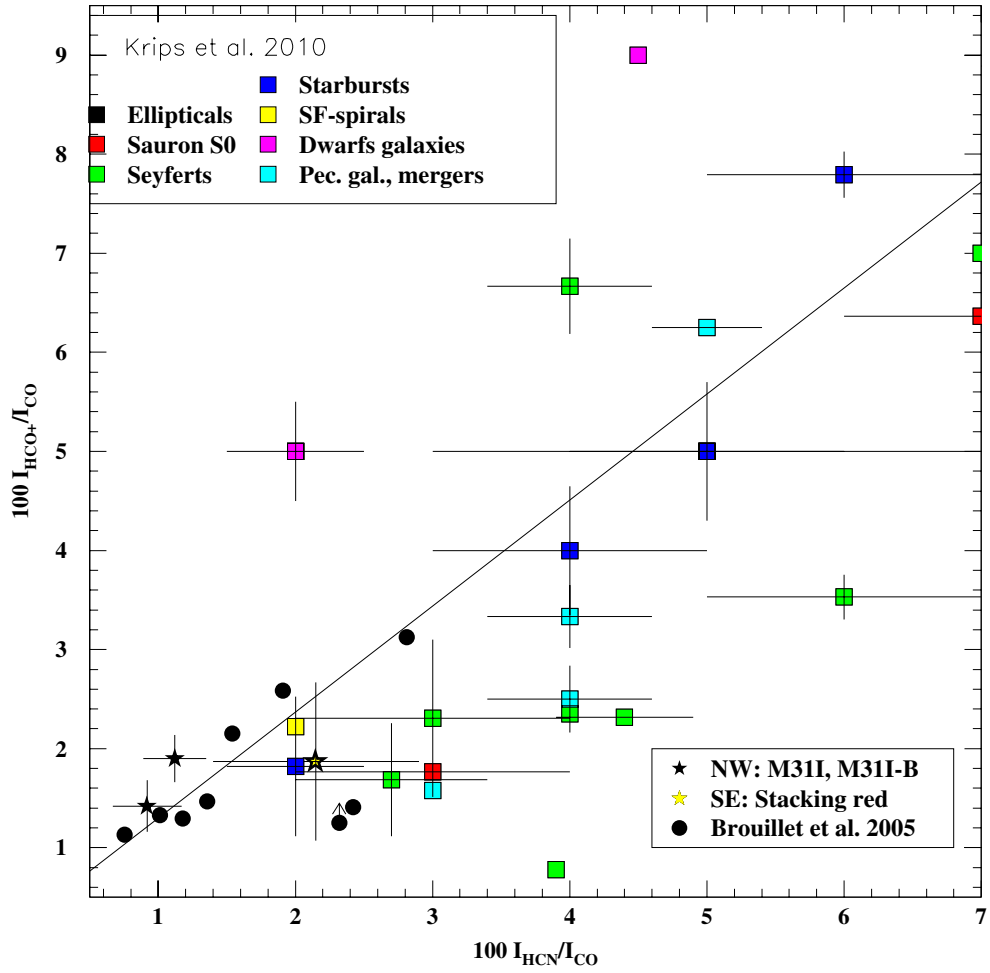

Fig. A.3. Comparison with other catalogues (2). HCO+/CO(1–0) line ratio versus HCN/CO line ratio. The two detections presented here (M31I and M31I-B) are superimposed on previous measurements, namely: detections across M31's main disc by Brouillet et al. (2005) and a compilation of various types of galaxies from Krips et al. (2010). The ^{12}CO(2–1) measurements presented here have been corrected by a CO 2–1/1–0 line ratio of 0.8, as measured in Melchior & Combes (2011) in a complex M31G within 10 and 30″ from the observed positions. The line indicates the best fit provided by Brouillet et al. (2005) for M31's main disc. Our points are systematically above the best fit they provide, suggesting an excess of HCO+. The overall distribution of Krips et al. (2010) does not exhibit any clear pattern.

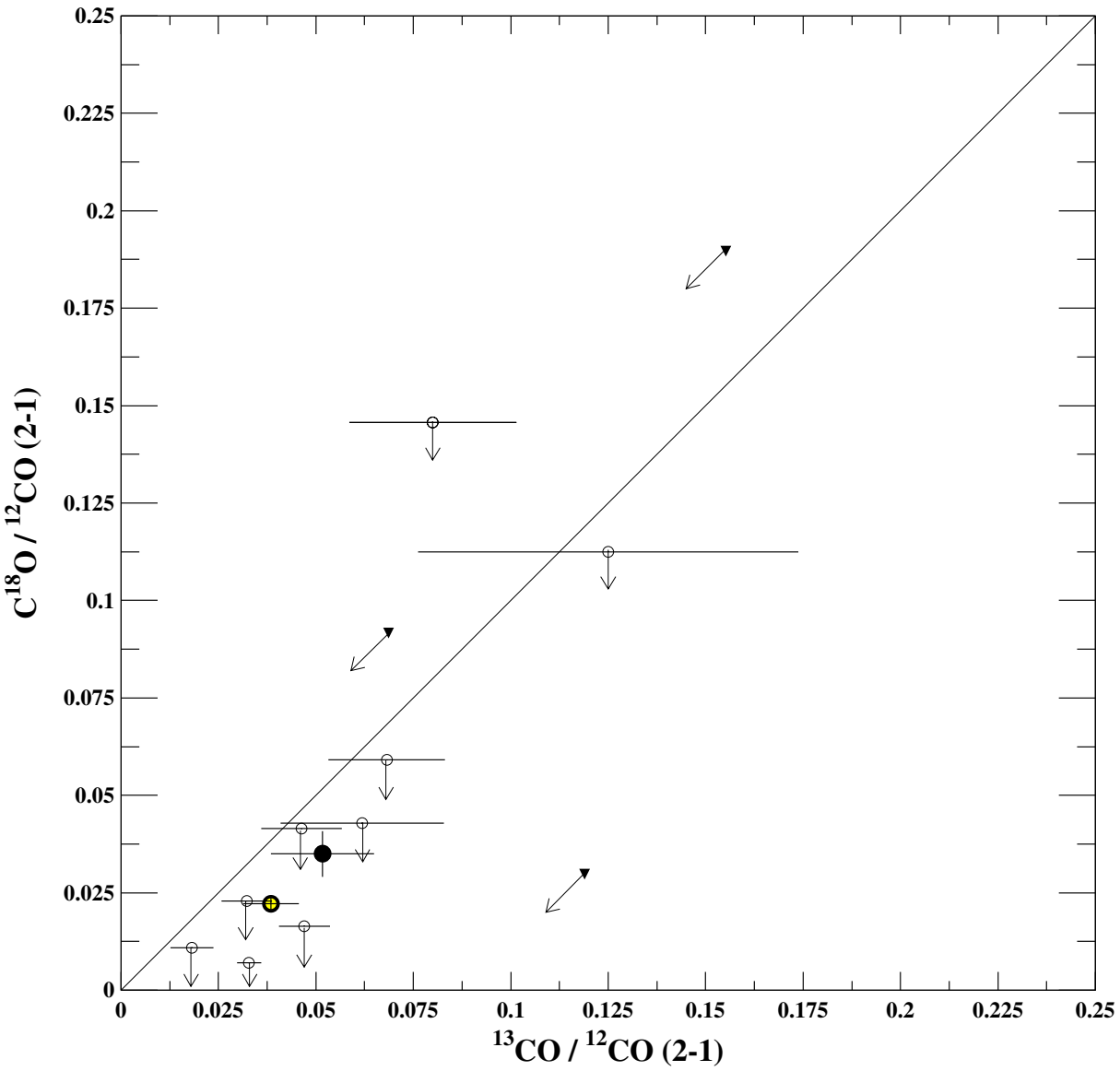

Fig. A.4. $C^{18}O/^{12}CO$ (2–1) line ratios versus the $^{13}CO/^{12}CO$(2–1) line ratios presented in this paper. Arrows indicated 3σ upper limits. The full black (empty yellow) point with error bars corresponds to our direct detection (our red stack detection). The line indicates a slope 1.

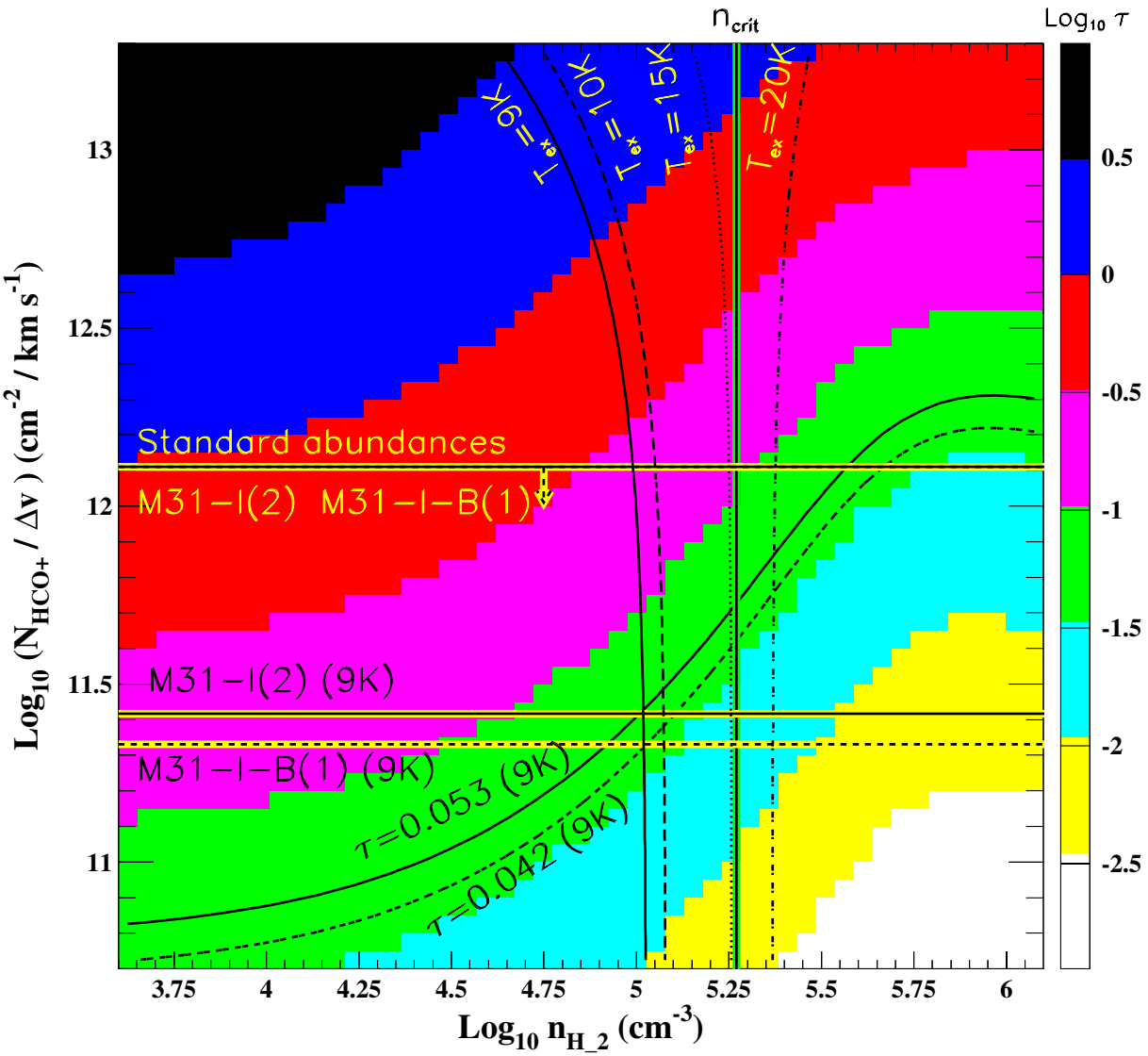

Fig. A.5. Main physical parameters corresponding to the HCO+(1–0) gas observed in M31-I(2) and M31-I-B(1). The optical depths are shown as function of the HCO+(1–0) column density (per km s^{-1}) and the molecular hydrogen density $n_{\mathrm{H_2}}$. The vertical (green) line indicates the critical density computed for a collisional temperature of 20 K (see Table 3). The lower horizontal full (dashed) line shows column densities measured for M31-I(2) (M31-I-B(1)) at 8 K. The upper horizontal line corresponds to the column densities computed with standard abundances (Bergin et al. 1995) and the corresponding molecular hydrogen column densities. For M31-I-B(1), we derive an upper limit as the molecular hydrogen column density is only available for a smaller beam (see Table A.1) and we expect some dilution of the signal, as is the case for M31-I(2). The contour levels correspond to excitation temperatures of 9 K (full line), 10 K (dashed line), 15 K (dotted line), and 20 K (dash-dotted line).